IN-SITU SCANNING ELECTRON MICROSCOPY (SEM) OBSERVATIONS OF THE TENSILE AND TENSILE-CREEP DEFORMATION OF TI-8AL-1MO-1V (WT.%) ALLOY

By

Indraroop Ghosh Dastidar

A THESIS

Submitted to
Michigan State University
in partial fulfillment of the requirements
for the degree of

Materials Science and Engineering-Master of Science

2014

ABSTRACT

IN-SITU SCANNING ELECTRON MICROSCOPY (SEM) OBSERVATIONS OF THE TENSILE AND TENSILE-CREEP DEFORMATION OF TI-8AL-1MO-1V (WT.%) ALLOY

By

Indraroop Ghosh Dastidar

Titanium (Ti) and titanium alloys (Ti alloys) are attractive for structural applications, such as in the aerospace and automotive industries due to their high specific strength, excellent corrosion resistance and good ability to withstand elevated temperatures. To develop Ti alloys with better mechanical properties, it is necessary to comprehend the deformation behavior of available Ti alloys.

Previous studies performed by another graduate student, Dr. Hongmei Li, involved investigation of the deformation behavior of commercially pure (CP) Ti, Ti-5Al-2.5Sn (wt.%), Ti-3Al-2.5V (wt.%) and Ti-6Al-4V (wt.%) alloys. The current thesis focused on investigating the deformation behavior of Ti-8Al-1Mo-1V (wt.%). *In-situ* tensile and tensile-creep experiments were performed at temperatures ranging from room temperature (RT) to 650^{O}C inside a scanning electron microscope (SEM), which allowed for the observation of the surface deformation evolution. Electron Back Scattered Diffraction (EBSD) was used to identify the distribution of the active deformation systems.

In this thesis efforts were made to characterize the various deformation modes of the Ti-8Al-1Mo-1V (wt.%) alloy as a function of the testing conditions (stress and temperature). It was observed that prismatic slip made up the majority of the observed slip systems during the RT tensile deformation, while basal and prismatic slip were almost equally active during the 455^{O}C tensile deformation. Grain boundary ledges were observed during the elevated temperature tensile-creep deformation and from this observation it was suggested that grain boundary sliding was an active deformation mode.

This work also involved estimating the Critical Resolved Shear Stress (CRSS) ratios of the α-phase deformation modes. The CRSS ratios were compared with the CRSS ratios of CP Ti and other Ti alloys. Overall, this work was intended to add more data to the scientific literature of Ti alloys in order to better comprehend their deformation modes, so as to design and develop higher performance Ti alloys.

ACKNOWLEDGEMENTS

First, I would like to thank my thesis advisor Dr. Carl Boehlert for his invaluable guidance throughout my masters' work. He motivated me to keep focused on my work and moreover taught me to do something that will be beneficial for the society. Besides, as a person, he was always a friend to me and helped me to overcome tough situations. It was because of him that I got the opportunity to present my work at the MS&T Conference'13 (Oct'2013), Montreal, Canada just 10 months after starting my graduate studies.

I would also like to thank my co-advisor Dr. Thomas Bieler. He taught me a many interesting things about crystallography which helped me a lot for this work. His enthusiasm and passion for exploring new areas in science and research inspired me through this work and will continue inspiring me in my future work.

I am also thankful to Dr. Martin Crimp and Dr. Philip Eisenlohr for the insightful discussion during our weekly group meetings. Those meeting often ended up in finding ways to chase difficult research questions.

I am also indebted to my professors in the Department of Metallurgical and Materials Engineering at the National Institute of Technology Durgapur (NIT Dgp), India, especially Prof. Rabindra Nath Ray (my undergraduate thesis advisor) and Dr. Joydeep Maity for motivating me to delve deep into things that interests me, providing me with valuable knowledge in various areas of Materials Science, which built a strong foundation in me to tackle hard research questions. I would like to thank Dr. Karabi Das at the Indian Institute of Technology Kharagpur (IIT Kgp), India for providing me the internship opportunity to utilize my skills in solving problems in Materials Science, at IIT Kgp for two consecutive summers (2010 and 2011).

I would also like to thank the current and former members in Dr. Boehlert's group, who have directly and indirectly helped me during my thesis work, including Dr. Hongmei Li, Mr. Ajith Chakkedath, Ms. Uchechi Okeke and Ms. Aida Amroussia. I would also like to thank Dr. Per Askeland for his assistance with using the SEMs. I would also like to thank those who sacrificed their time to help me in any respect during the completion of my degree.

I would like to acknowledge Dr. Adam Pilchak of the Air Force Laboratory at Wright Patterson Air Force Base (Dayton, Ohio) for providing the material for this work, the funding for this research was provided by US Department of Energy, Office of Basic Energy Science through grant No. DE-FG02-09ER46637.

Finally I would like to thank my friends at MSU, Prianca Bhaduri, Prakash Kumar Shee, Rajib Mandal, Subhayu Mukherjee, Tias Maity, Saptarshi Mukherjee and Portia Banerjee for making me feel at home although being 8000 miles away from home. Without them, life at MSU would not have been so wonderful, and I will cherish those moments throughout the rest of my life. My deepest gratitude to my parents, my brother, and my best friends Sandipan Banerjee, Abhishek Banerjee and Subhajit Saha for their selfless love and support, and for their understanding and belief in me. Cheers to all of you. Lastly I would like to mention that pursuing a degree from the USA was a dream that I saw when I was in standard III-IV, and is one of my biggest dream, so final words are "One of my biggest dreams has finally come true." Thank you USA, and at the same time thank you India for bringing me up, providing me with the resources needed to get established in life.

TABLES OF CONTENTS

LIST OF TABLES

LIST OF FIGURES

KEYS TO SYMBOLS AND ABBREVIATIONS

2D	Two-dimensional
Al	Aluminum
Approx.	Approximate
ASTM	American society for testing and materials
b	Dislocation slip direction
BCC	Body center cubic
CP	Commercially pure
Cr	Chromium
CRSS	Critical resolved shear stress
Do	Pre-exponential constants for diffusion
D	Diffusivity
EBSD	Electron backscattered diffraction
EDM	Electrodischarge machined
ε	Engineering strain
Fe	Iron
GBS	Grain boundary sliding
HCP	Hexagonal closed-packed
ICP-MS	Inductively coupled plasma mass spectroscopy
IPF	Inverse pole figure
m	Schmid factor
Mg	Magnesium
Mo	Molybdenum

$\boldsymbol{n}$	Dislocation slip/twin plane normal
N	Nitrogen
Ni	Nickel
O	Oxygen
pct.	Percent
$\boldsymbol{\sigma}$	Applied stress
SE	Secondary electron
SEM	Scanning electron microscopy
SiC	Silicon carbide
Q	Activation energy
R	Universal gas constant
RT	Ambient temperature/Room Temperature
Ti	Titanium
Tin	Sn
UTS	Ultimate tensile stress
V	Vanadium
wt.%	Weight percent
XRD	X-ray diffraction
YS	Yield stress
Zr	Zirconium

CHAPTER 1

INTRODUCTION, BACKGROUND AND MOTIVATION

1.1 Titanium and Titanium alloys

Titanium was first identified as a new and unknown metallic element by Gregor in England (1791), and was named Titanium by Klapproth (1795) in Germany after the Titans of the Greek mythology [Lütjering et al. 2003]. Compared to other structural metallic metals based on iron (Fe), nickel (Ni), aluminum (Al), and magnesium (Mg), titanium (Ti) stands out due to its high strength-density ratio, high corrosion resistance and its excellent ability to withstand high temperatures owing to their high melting point [Leyens et al. 2003]. Some of the fundamental characteristics of Ti and its alloys are shown in table 1.1.

Table 1.1 Important Characteristics of Ti and Ti based alloys as compared to other structural metallic materials based on Fe, Ni, Al and Mg [Lütjering et al. 2003, Li 2013].

	Ti	Fe	Ni	Al	Mg
Melting Temperature (^{o}C)	1670	1538	1455	660	650
Room Temeprature Young's Modulus E (GPa)	115	215	200	72	45
Yield Stress (MPa)	1000	1000	1000	500	130
Density (g/cm^3)					
Comparative Corrosion Resistance	Very High	Low	Medium	High	Low
Comparative Reactivity with Oxygen	Very High	Low	Low	High	
Comparative Price of Metal	Very High	Low	High	Medium	Medium

Therefore, Ti and its alloys find applications primarily in two areas: corrosion resistant areas, such as the chemical industry, and in areas where weight-savings and high strength are important, such as in aircraft and aerospace applications.

1.2 Crystal Structure

Pure Ti is allotropic and at 882^{o}C undergoes an allotropic phase transformation from a body-centered cubic crystal structure (β phase, lattice parameter: *a*=0.332 nm) at higher temperatures to a hexagonal close-packed crystal structure (α phase, lattice parameters: *a*=0.295 nm and c=0.468 nm) at lower temperatures. This phase transformation follow following the Burger's relationship $\{0001\}_{\alpha}||\{110\}_{\beta}$, $<11\text{-}2\ 0>_{\alpha}||<111>_{\beta}$ [Lütjering et al. 2003, Leyens et al. 2006, Burgers 1934].

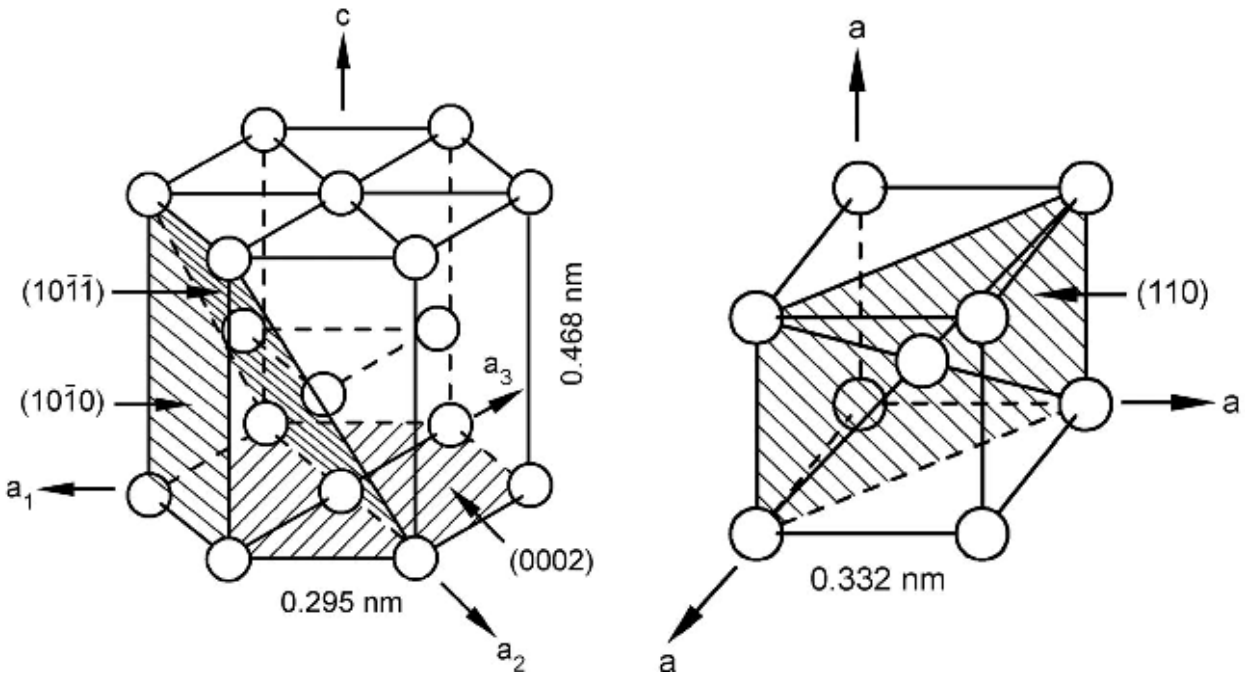

(a) (b)

Figure 1.1(a) Unit cell of α-phase and (b) unit cell of β-phase [Lütjering et al. 2003].

The in *c/a* ratio for pure α Ti is 1.587, which is a bit deviated from the ideal ratio of 1.633 for the hexagonal close-packed crystal structure [Yoo 1981]. With alloying, the phase transformation temperatures can be varied. For the hcp α-phase unit cell (Figure 1.1 (a)) there are three densely packed lattice planes, the basal {0002} plane, one of the three prismatic {1010} planes and one

of the six pyramidal {1011} planes, and for each of those planes the closed packed direction is <1120 >. The unit cell of the body centered cubic (bcc) β phase (Figure 1.1 (b)) has six most densely packed {110} lattice planes and for each of those planes there are two <111> closed packed directions.

1.3 Alloying Elements and Phase Diagrams

The alloying elements Ti alloys are generally categorized in three parts classified into three classes: α, α+β, and β alloys. Also, depending on the effect of the alloying element into the β-transus temperature, alloy elements are classified into α or β stabilizers, depending on their effect on the β-transus temperature.

For example increased content of Al, O, N and C increases the transus temperature, and hence they are called α-stabilizers (Figure 1.2).

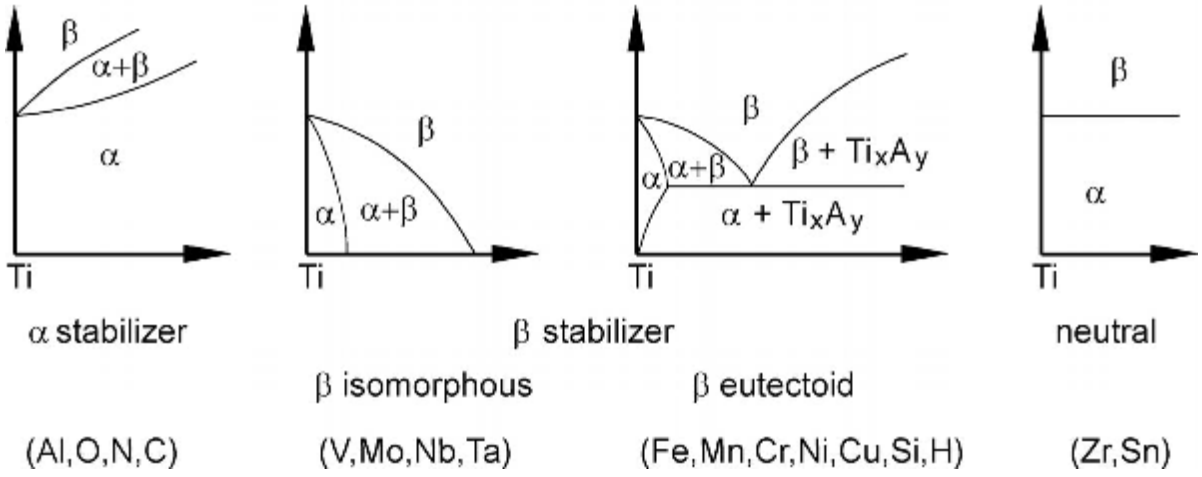

Figure 1.2: Effect of alloying elements on phase diagrams of Ti alloys (schematically) [Lütjering et al. 2003].

Depending on the type of solid solutions they form, the β stabilizing elements are divided into β isomorphous elements and β eutectoid forming elements (schematic of both types are shown in

Figure 1.2). Some of the widely used β-stabilizing elements in titanium alloys are V, Mo, and Nb, and an increased content of these elements increases the stability of the β-phase field by lowering the transus temperatures, sufficient concentrations of these elements make it possible to stabilize the β-phase even at room temperature (RT). There are some elements such as Zr, Hf and Sn, which do not have any significant effect on the β-transus temperature, and hence they are called neutral elements.

Since the alloy (Ti-8Al-1Mo-1V) used for this work has Al, Mo and V as alloying contents, the binary phase diagrams of these elements with Ti are introduced here.

1.3.1 Ti-Al Phase Diagram

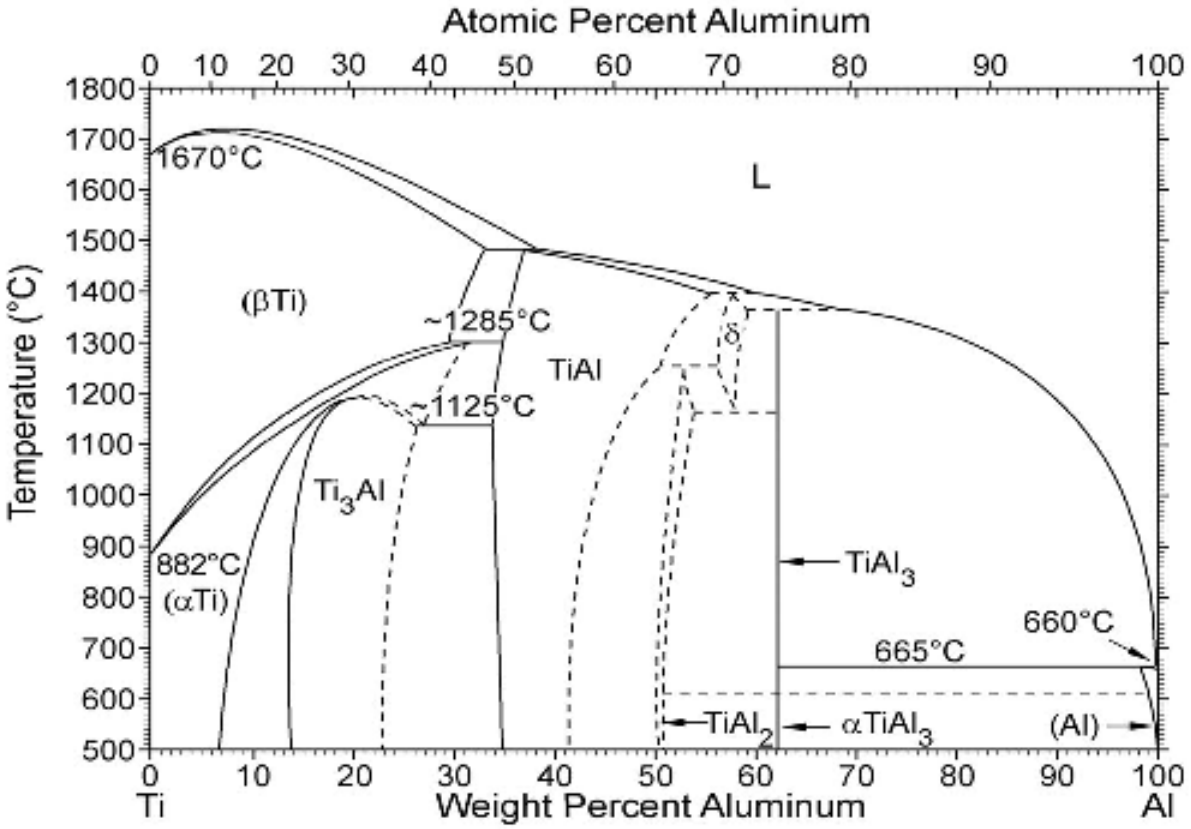

Figure 1.3: Ti-Al phase diagram [Lütjering et al. 2003].

Aluminum has been always an important alloying element of Ti alloys because it imparts strength to the material by solid-solution strengthening and it is an important α-stabilizer. The Ti-Al phase diagram is shown in Figure 1.3. With an increase in Al content, intermetallic compounds like the Ti_3Al (α_2) phase are formed. The Ti_3Al phase has a DO_{19} ordered hexagonal crystal structure.

Increased Al content results in an increase in the *c/a* ratio and leads to a more closed packed basal plane. Teer et al. [1977] has shown that increased Al content causes a reduction in both *a* and *c*. Their study shows that the *c/a* ratio can be varied from 1.587 to 1.61 with 40 wt.% Al [Figure 1.4].

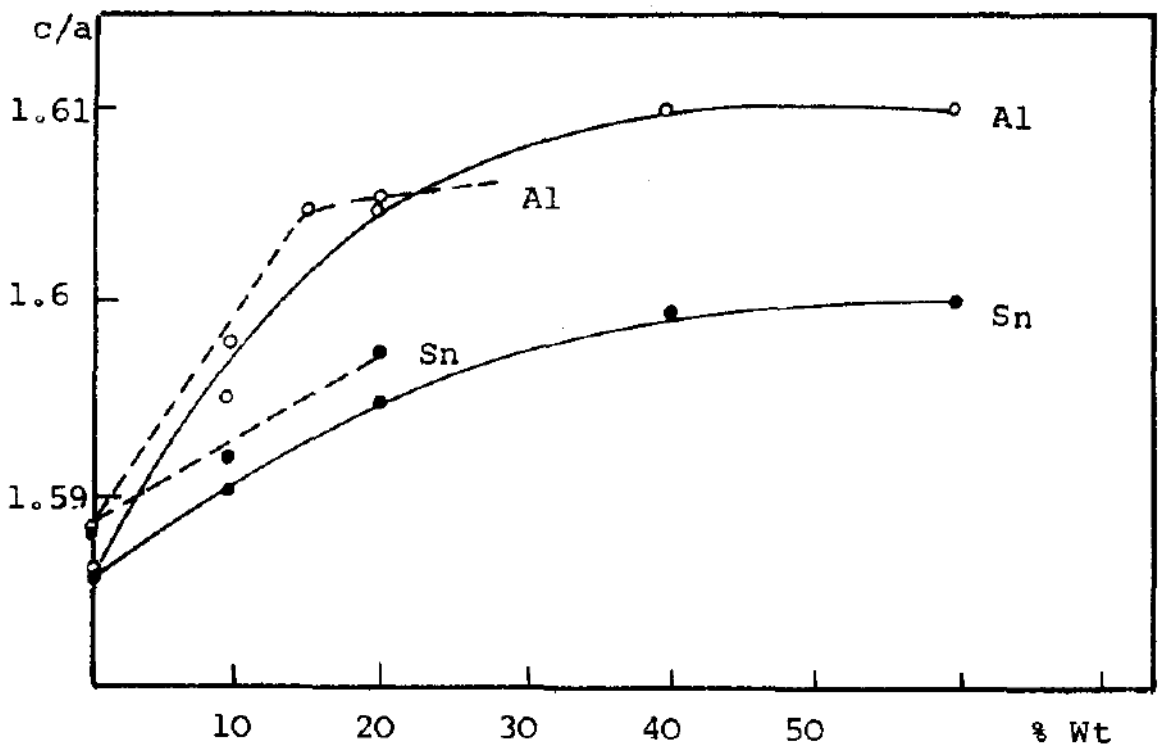

Figure 1.4 Plot showing *c/a* ratio in Ti as a function of Al and Sn content (wt%.) [Teer et al. 1977].

1.3.2 Ti-V Phase Diagram

Vanadium is a β-phase stabilizer for Ti alloys. Increased V content increases the strength of the alloy, and it also adds to other mechanical properties [Donachie 1988].

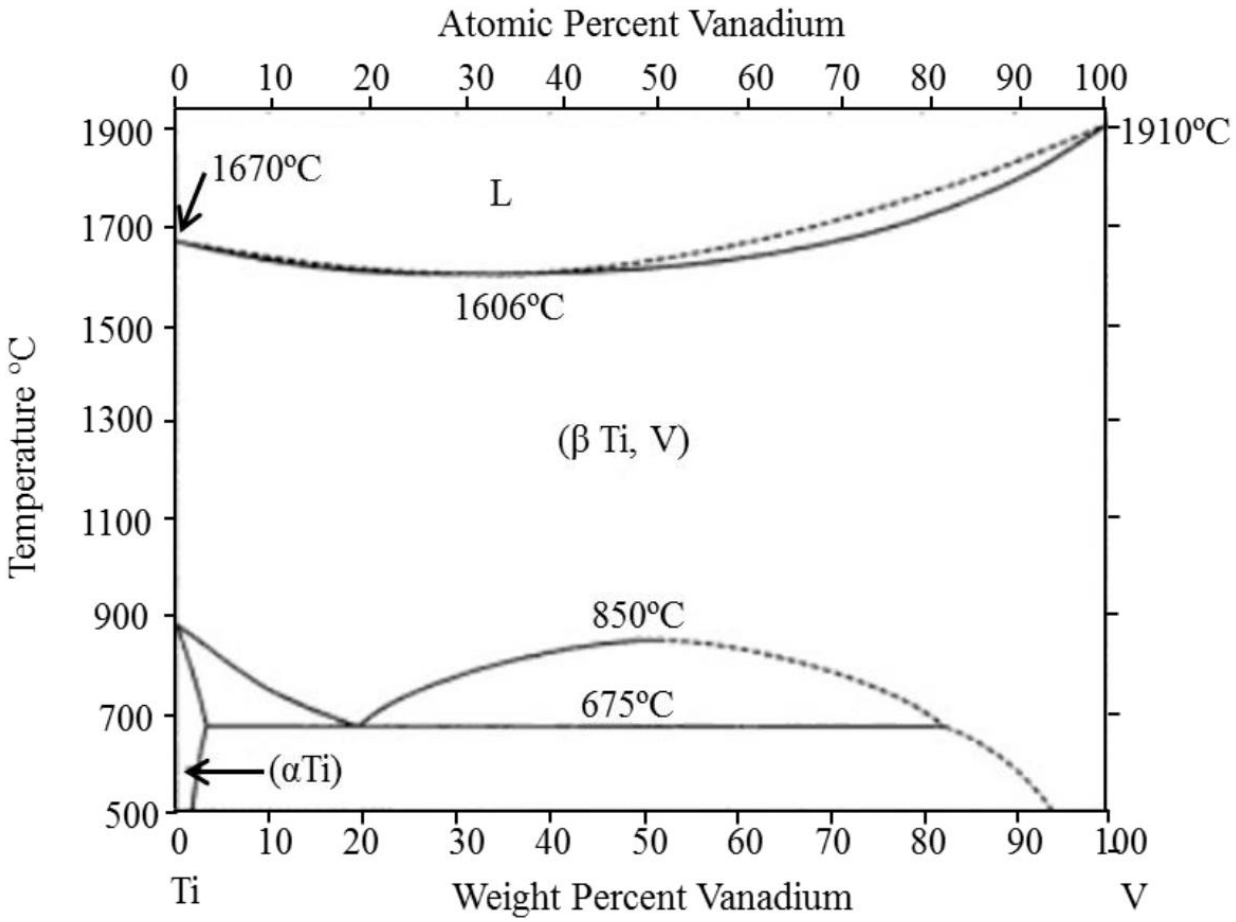

Figure 1.5 Ti-V phase diagram [Okamoto et al. 2000].

Vanadium has a similar atomic radius (0.171nm) to that of Ti (0.176nm) [Clementi et al. 1963]. Hence V does not cause much of a change in the *c/a* ratio. The Ti-V binary phase diagram is shown in Figure 1.5, and it shows no evidence of intermetallic compounds formation.

1.3.3 Ti-Mo Phase Diagram

Molybdenum is another β-stabilizing element, and the Ti-Mo binary phase is shown in Figure 1.6.

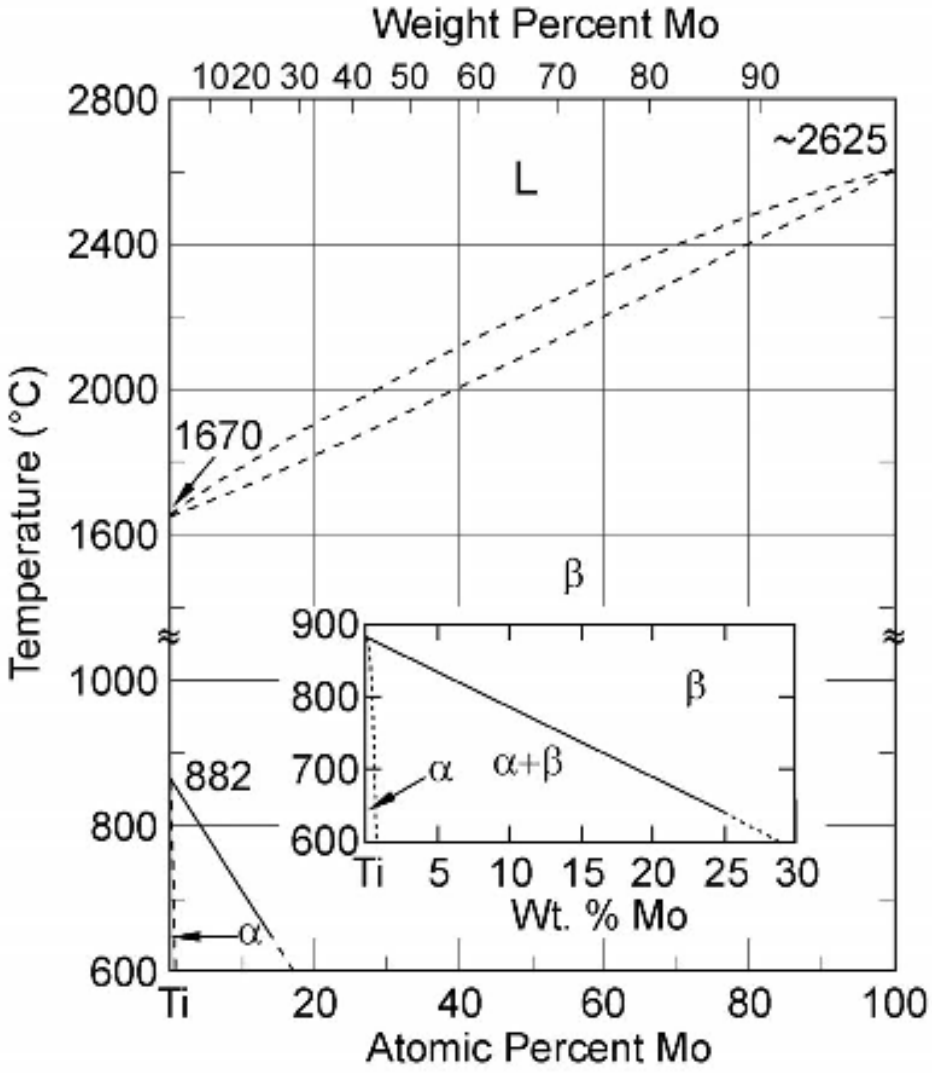

Figure 1.6 Ti-Mo phase diagram [Lütjering et al. 2003]

For Mo contents greater than 20 at.%, there exists a miscibility gap outside the (α + β) phase field. The solid solubility of Mo in the α-phase is very low (below 1at.%).

1.4 Deformation Mechanism

1.4.1 Slip Systems

The most common slip systems in HCP Ti are basal, prismatic, pyramidal <a>, and pyramidal <c+a> slip systems [Yoo 1981]. As per the von Mises criterion [von Mises 1913], five independent slip systems are necessary for general homogenous plastic deformation in a polycrystalline material.

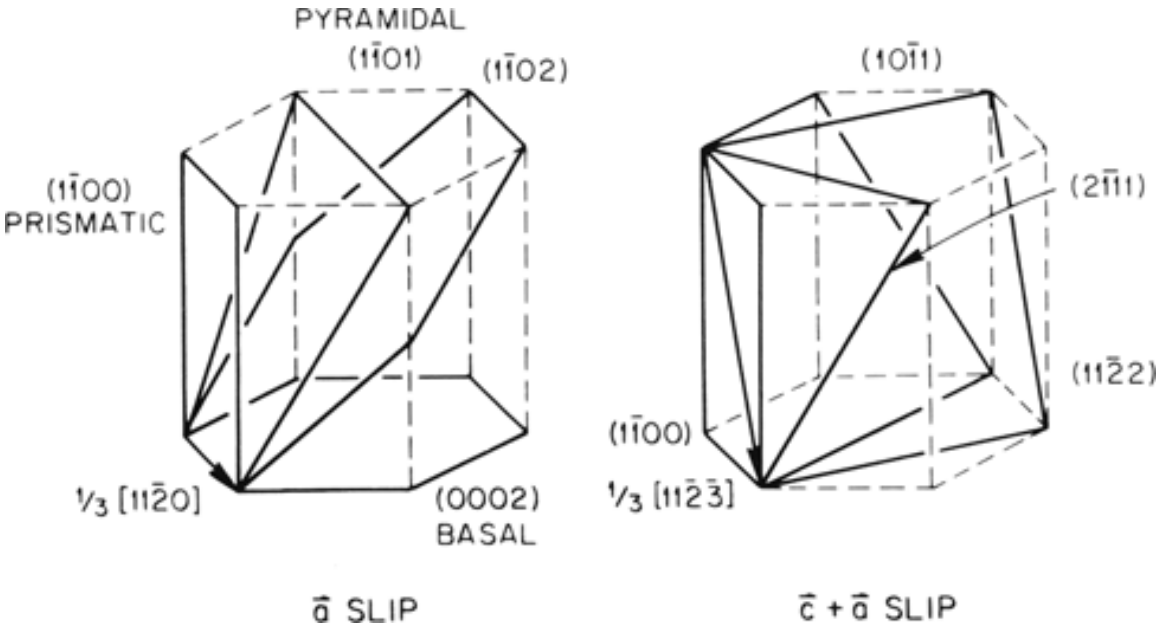

Figure l.7 Basal, prismatic, and pyramidal slip systems with **a** Burgers vector, and four possible pyramidal slip planes with *c* + *a* Burgers vector [Yoo 1981].

In the hcp crystal, *a*<11-20> and *c* + *a*<11-2-3> are the two most likely Burgers vectors. But there are three slip systems with the *a* type Burgers vector. Therefore in order to satisfy the von Mises criterion for accommodating plastic deformation, <*c*+*a*> slip systems must be activated in addition to the three *a*-type slip systems.

The ease of slip on a particular system is quantified by the CRSS, which has been observed to vary significantly for Ti and Ti alloys depending on alloying content and temperature [Li 2013, Chan 2004]. Prismatic slip was observed as the most easily activated slip system in CP Ti, while basal slip has been observed to be more easily activated in the near-α and α+β alloys [Williams et al. 2002, Zaefferer 2003, Bridier et al. 2005,]. Teer *et al.* [1977] has suggested that a more close-packed basal plane is expected in the alloys containing Al and Sn compared to CP Ti, suggesting easy activation of basal slip for alloys containing these elements. Williams et al. [2002] suggested increased temperature decreases the CRSS of both basal and prismatic slip for single crystal α Ti-Al alloys with compositions ranging from Ti-1.4Al to Ti-6.6Al. However the decrease in CRSS for basal slip is more dramatic than that for prismatic slip.

1.4.2 Twinning

In addition to dislocation slip, twinning is also another deformation mode in crystalline solids. In tension, {10-12} <-1011> T1 twinning and {11-21} <-1-126> T2 twinning may be activated [Christian et al.1995]. While during compression,{1122} <11-2-3> C1 twinning and {10-11}<10-12 > C2 twinning may be activated. [Christian et al. 1995]. The four different twinning modes mentioned as shown in Figure 1.8. When the maximum principal stress direction is oriented close to the crystal c-axis, pyramidal <c+a> and/or twinning systems generally become favorable as they will have high Schmid factors. Every twinning mode has a unique misorientation angle and rotation axis with respect to the parent orientation [Christian et al. 1995], along with a twinning shear which is defined as the shear required to restore the lattice in a new orientation [Bevis et al. 1968], as summarized in Table 1.2 [Christian et al. 1995]. The lower the value of the twin shear, the easier it is for the twin to form.

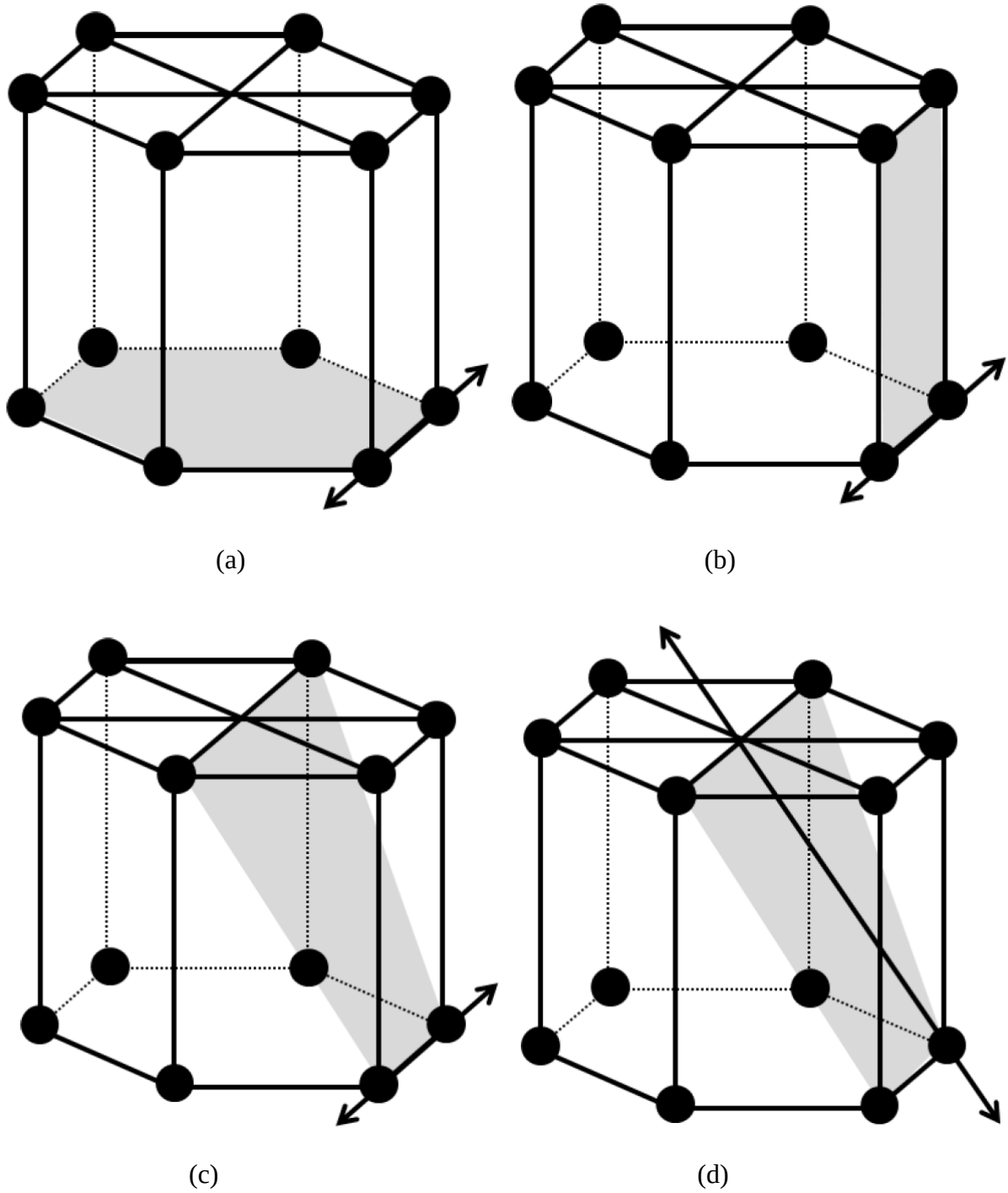

Figure 1.8 (a) {10-12} <-1011> T1 twinning, (b) {11-21} <11-26 > T2 twinning, (c) {11-22} <11-2-3> C1 twinning, (d) {1011}<1012 > C2 twinning systems in HCP Ti. The arrows only indicate the twinning directions, not the magnitudes of the twinning [Christian et al. 1995].

Table 1.2 Deformation twinning modes in HCP Ti [Christian et al. 1995].

Mode	Twinning system	Misorientation	Twin shear
T1	{10-12} <-1011>	85^o <1-210>	0.171
T2	{11-21} <-1-126>	35^o <1-100>	0.629
C1	{11-22} <11-2-3>	65^o <-1100>	0.229
C2	{10-10} <10-12>	54^o <-12-10>	0.101

In titanium alloys twinning is often an important deformation mode. For CP-Ti, T1 tension twins have been the most frequently observed twin system due to their low value of twin shear. Generally twinning has been observed in grains exhibiting high Schmid factors for twinning systems [Li et al. 2013].

However, several other factors, including temperature and alloying additions, have also been reported to affect the twinning activation. It has been observed that a low O content is favorable for twinning activity [Zaefferer 2003]. It has also been reported that an increased Al content and increased temperature decreases twinning activity [Williams et al. 2002, Li 2013]. Twinning has been observed in CP-Ti during the temperature range of 296K-728K [Li 2013]. Comparison of the twinning activity for four commercial Ti alloys (CP Ti, Ti-5Al-2.5Sn, Ti-3Al-2.5V and Ti-6Al-4V) show that generally twinning gets less favored for alloys containing more Al content [Li 2013]. Comparison of the twinning activity for a particular alloy at different temperatures suggested that increased temperature results in less twinning activity [Li 2013]. Paton et al. [1976] stated that Ti alloys containing at least 6 wt.% Al do not twin, even at temperatures at low as 100K.

1.4.3 Grain Boundary Sliding

Grain boundary sliding (GBS) is a shear process where grains in polycrystalline microstructures move relative to each other along the grain boundary interface [Dieter 1986]. According to Ball and Hutchison [Ball A. and Hutchinson M.M. 1969], GBS occurs by the glide and climb (at the grain boundaries) of dislocations. Dislocations emitted from the ledges of the grain boundaries travel within the grain to the opposite grain boundary, where they pile-up. This in turn creates a back stress preventing further emission of dislocations from the ledge. For more deformation to occur that back stress needs to be relieved by dislocation climb. Figure 1.9 provides a schematic of the process of GBS proposed by Ball and Hutchison (1969).

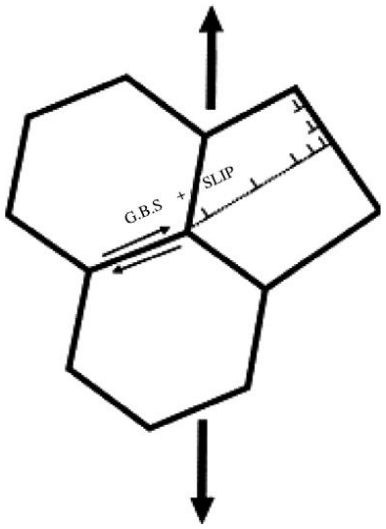

Figure 1.9 Mechanism of grain boundary sliding as per the Ball–Hutchison model [Fisher et al. 1964].

GBS is an active deformation mode in Ti alloys especially at elevated temperatures [Gollapudi et al. 2008, Li et al. 2012]. An example of GBS during elevated temperature creep of a commercial Ti alloy is given in Figure 1.10.

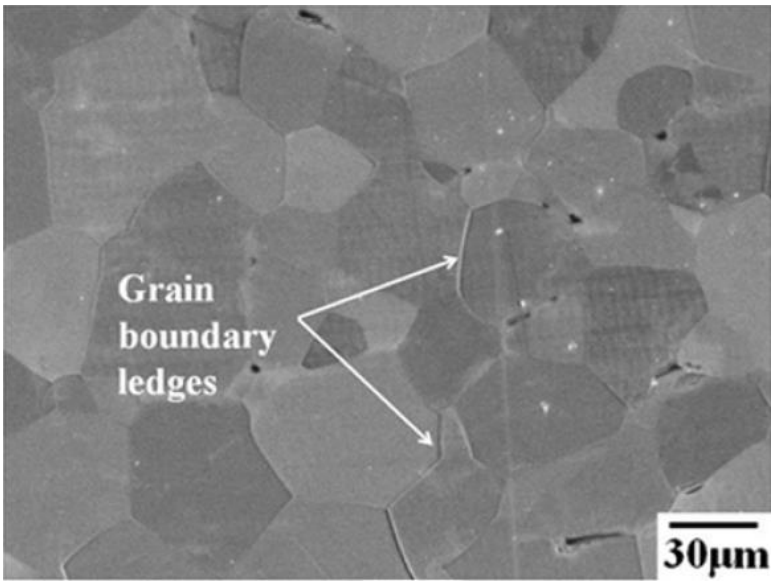

Figure 1.10 Observations of grain boundary ledges during 763K, 200 MPa creep of a Ti-5Al-2.5Sn (wt%.) alloy [Li et al. 2012].

1.4.4 Estimation of CRSS ratios for active slip systems

Slip system activity of CP-Ti and Ti-alloys has been studied by several groups over the years [Paton et al. 1970, Williams et al. 2002, Yoo 1981, Chan 2004, Zaefferer 2004, Bieler et al. 2002, Bridier et al. 2008, Li et al. 2012, Li et al. 2013]. Compared to an ideally-packed hexagonal crystal structure, the reduced c/a ratio of pure α-Ti leads to a larger spacing between the prism planes. This causes the packing density of the prism planes to increase relative to the basal planes, thus favoring slip on prism planes rather than on basal planes [Teer et al. 1977]. The plastic anisotropic nature of polycrystalline hcp metals are a result of well-developed deformation texture originating from the limited number of slip and twinning systems. In order to characterize the plastic anisotropy, it is necessary to estimate the shear stresses needed for each of those deformation mechanisms [Paton et al. 1970]. People have estimated the CRSS ratios of the different slip systems for CP-Ti and different Ti alloys (single crystal and poly-

crystals) under different testing conditions [Gong et al. 2009, Zaefferer et al. 2003, Salem et al. 2005, Balasubramanium et al. 2002, Chan et al. 2004, Bieler et al. 2002]. However there is no consensus on the CRSS ratios of different Ti alloys, as variations in the CRSS ratios are observed for different Ti alloys. In addition, results by different groups are sometimes different for the same alloy [Li et al. 2013]. It is important to note that testing conditions have an effect on the CRSS ratios. Hence to compare CRSS ratios for different alloys, they should be tested under the same conditions. Li [2013] estimated the basal: prism: pyramidal<a>: pyramidal<c+a> CRSS ratios at RT for CP-Ti (1: 0.28: 7.1: 6.3), Ti-5Al-2.5Sn (1: 0.81: 19.1: 35.5), Ti-3Al-2.5V (1: 0.16: 0.81: 5.7) and Ti-6Al-4V (1: 1.2: 13.2: 38) using surface slip trace analysis on samples deformed to different strain levels in tension. In the current work, tensile tests on Ti-8Al-1Mo-1V (wt.%) were performed under the conditions similar to those used by Li [2013], and a comparison of the CRSS ratios between Ti-8Al-1Mo-1V and different Ti alloys under identical testing conditions are provided and discussed. CRSS for twinning systems have not been evaluated since no twinning was observed during the room temperature tensile tests of Ti-8Al-1Mo-1V, and no twinning analysis have been done for the elevated temperature tensile and tensile creep tests.

1.5 *In-Situ* Mechanical Testing

1.5.1 *In-Situ* Tensile Testing

Tensile testing is done to find the strength of a material under different testing conditions. From tensile testing, the stress vs strain curve of any material can be obtained at any temperature. Studying the surface deformation of a well-polished specimen under different testing conditions can provide useful information about the deformation behavior.

Tensile testing shows the variation in yield stress (YS) and ultimate tensile stress (UTS) of materials possessing different microstructure. Miller *et al.* [1987] has shown how YS and UTS vary for Ti-6Al-2Nb-1Ta-0.8Mo as a function of processing, which results in different microstructures. The stress-strain curve provides a measure of the effect of alloy composition on the mechanical behavior of a material. Paton *et al.* [1970] used tensile tests to find the effect of crystallographic orientation on slip system activation of Ti single crystals.

In order to characterize the surface deformation evolution of a specimen, *in-situ* experiments can be performed. Li *et al.* [2012] characterized the slip and twinning deformation systems as well as GBS of a near-α Ti-5Al-2.5Sn (wt.%) for the temperature range of 296-763K using *in-situ* tensile tests. Their work has shown the relative activation of different slip systems under different temperatures, and they captured the evolution of slip lines and grain boundary ledges on a given microstructural patch. Li [2013] also characterized the deformation modes of a near-α Ti-3Al-2.5V (wt.%) under different temperatures using *in-situ* tensile experiments. Having a measure of the relative activation of slip systems under different temperatures for a material, the CRSS ratios at a particular temperature for a material can be computed and compared with similar alloys to estimate the initiation and progression of a particular system (eg. Ti system

means family of Ti and Ti alloys) as a function of temperature and alloying composition [Li et al. 2013].

The motivation of using *in-situ* tensile tests for this work was to systematically characterize the surface deformation evolution of Ti-8Al-1Mo-1V (wt.%). The deformation mode distribution aided the calculation of the CRSS ratios of four slip systems (basal, prism, pyramidal<c+a> and pyramidal<a>) in α-hcp Ti during different testing conditions. Efforts were also been made to characterize GBS and cracking which developed during the course of testing the alloy at various temperatures and applied stresses.

1.5.2 *In-Situ* Tensile Creep Testing

Creep is deformation under constant load. The term 'creep' is used to identify the slow deformation observed in materials under the application of a constant (below the yield stress) load particularly at higher temperatures. While metals and alloys have been observed to creep at very low temperatures, generally creep occurs at higher temperatures. With increased temperature, metals have been observed to lose strength. An important reason for this issue is the increase in mobility of atoms with temperature i.e. diffusion of atoms/vacancies or dislocations. Other significant contributors to this issue are the movement of dislocations by climb or glide and sliding of grains past one another.

Often, prolonged exposure to high temperature leads to microstructural instabilities for metals. Examples of this are overaging in age-hardening alloys, while interaction of a metal with its environment at high temperature also causes deformation. Modern industries, especially the aviation and automotive industries, demand materials that can withstand high temperature with no significant loss in strength. In order to better creep resistant materials, a deep understanding

of the deformation behavior and mechanisms of different alloys under different conditions is required.

Gollapudi *et al.* [2008] studied the creep behavior of Ti-3Al-2.5V (wt.%) under a wide range of stresses and temperatures, and they characterized the deformation modes observed as a function of the testing parameters (i.e. stress and temperature). Hayes *et al.* [2002] and Thiessen *et al.* [1990] studied the effect of the alloying element content on the creep deformation behavior of Ti-6Al-2Sn-4Zr-2Mo. Es-Souni [2001] provided a comparison of the creep deformation behavior of three commercially-available Ti alloys (IMI 834, IMI 829 and IMI 685), and this would give an insight on the effect of composition and microstructure on the creep mechanisms.

Like *in-situ* tensile tests, *in-situ* tensile-creep tests allow for the capture of the deformation evolution under an applied load at a constant temperature. Li *et al.* [2012] quantified the distribution of the different deformation modes in a Ti-5Al-2.5Sn (wt.%) as a function of stress and temperature. Li [2013] also characterized the distribution of the different deformation modes in various other Ti alloys during tension-creep testing.

The motivation behind doing *in-situ* tensile-creep tests for this work was to characterize the distribution of the different deformation modes in Ti-8Al-1Mo-1V(wt.%) as a function of testing conditions (i.e stress, temperature and loading rate). The effects of stress and temperature on the active slip system distributions are discussed and efforts have been made to characterize the GBS and cracking activity as a function of stress and temperature. The CRSS ratios have been computed using a novel methodology [Li et al. 2013].

1.6 Work Performed

In this thesis work, the deformation behavior of a Ti-8Al-1Mo-1V (wt.%) alloy was investigated. The material was supplied by Dr. Adam Pilchak, of the Air Force Research Laboratory, Wright Patterson Air Force Base, Dayton, Ohio.

Chapter 1 provides a brief overview of the fundamental properties of Ti and Ti alloys.
In Chapter 2, the materials and experimental procedures used in this thesis work are described. This chapter includes information about the bulk alloy composition. In, addition this chapter covers details of the experimental set-up for the *in-situ* tensile experiments, methods for the slip trace analysis and Schmid factor calculations, and lastly the methodology used for estimating the CRSS ratios of the active slip systems.
In Chapter 3, the results from the microstructure and texture characterization, the *in-situ* tensile experiments, and the *in-situ* tensile-creep experiments are presented. The grain size was measured using the line-intercept method based on the secondary electron (SE) [ASTM 2004], and the texture was characterized for each specimen using electron backscattered diffraction (EBSD). *In-situ* tensile tests were conducted on the material at temperatures ranging from 25^{o}C-650^{o}C. The surface deformation evolution during each test was captured by SEM images acquired throughout the tests. *In-situ* tensile-creep tests were performed at 370^{o}C and 455^{o}C at constant stress levels. EBSD was performed for all the samples (tensile and tensile-creep) both before and after deformation. Results for the slip trace analysis for every test were presented, and the CRSS ratios for the active slip systems for every test were estimated. Efforts have been made to characterize the deformation behavior as functions of texture, composition and testing conditions.

In Chapter 4, the conclusions of this thesis work are presented and potential future work is suggested.

CHAPTER 2

EXPERIMENTAL PROCEDURES

2.1 Material

A Ti-8Al-1Mo-1V near α-alloy was investigated. The material was provided by Dr. A.L. Pilchak of the Air Force Research Laboratory, Wright Patterson Air Force Base, Dayton, Ohio. The material provided was in the form of a semi-circle (see Figure 2.1), that was obtained from a billet prepared by TIMET and was 12.7 cm in diameter.

The bulk chemical composition of the alloy was measured using inductively coupled plasma mass spectrometry (ICP-MS) by NSL Analytical (Cleveland, OH). The measured bulk chemical composition of the alloy is presented in Table 2.1.

Table 2.1 Chemical composition of the as-received billet (wt.% in descending order).

Al	V	Mo	O	N	Ti
7.75	1.00	0.97	0.11	0.0027	Balance

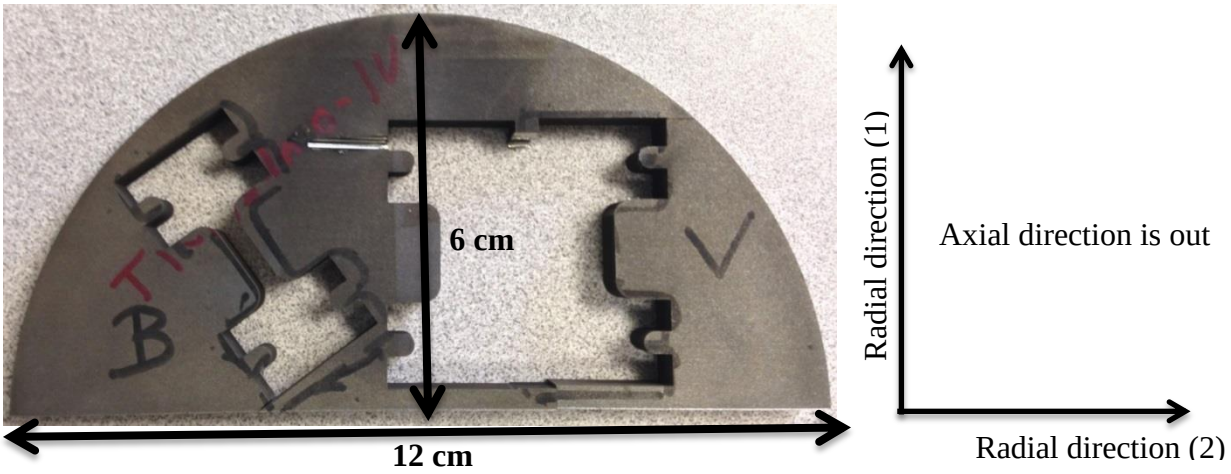

Figure 2.1 An image of the as-received semi-circle bar extracted from the Ti-8Al-1Mo-1V billet, from which samples were cut for mechanical tests. The radial and axial directions are also shown.

2.2 Microstructural characterization

2.2.1 Metallography preparation

After the mechanical test samples were cut, they were mechanically polished. The specimens were first polished using silicon carbide (SiC) grinding papers through 400, 600, 1200, 2400, and 4000 grits, sequentially, with each step taking around 5 to 10 minutes. Water was used to rinse the specimens before moving to the next grinding step. For the final polishing step, a solution of five parts colloidal silica with 0.06μm particle size and one part 30% hydrogen peroxide was used. This step normally took around 2-3 hours of continuous polishing. The polishing cloth used in this step was purchased from Buehler with catalog No. M500-12PS. After polishing was completed, water was used to rinse away the colloidal silica. Finally, the specimens were ultrasonically cleaned in acetone and methanol, respectively, to remove the residual colloidal silica on the specimens' surfaces.

2.2.2 Scanning electron microscopy

The microstructure of the alloy investigated was characterized using scanning electron microscopy (SEM). The SEM used in this work was a field emission gun Tescan Mira3 SEM, which is located in room 1130 of the Engineering Building at Michigan State University. Secondary Electron (SE) images were acquired before, during and after the experiments. These images were used to determine the phase volume fractions and grain sizes. The α phase of the Ti alloys evaluated in this study appeared dark or grey in the SEM images due to its low average atomic number (Al is the most common α-phase stabilizer and it has an atomic number of 13) while the β-phase appeared brighter because it is enriched with V (V is the most common β stabilizer and it has an atomic number of 23) [Boyer et al. 1994]. Adobe Photoshop software was used to measure the phase volume fractions present. The material exhibited equiaxed α-grains, and the grain sizes were measured using the line-intercept method [ASTM 2004].

2.2.3 EBSD analysis

After the metallographic polishing, EBSD orientation mapping was performed at selected areas of the *in-situ* gage section of the samples both prior to and after deformation. A razor blade scratch was intentionally imposed on the middle of the gage section of the samples as a reference line for identifying the EBSD scan areas (see Figure 2.2).

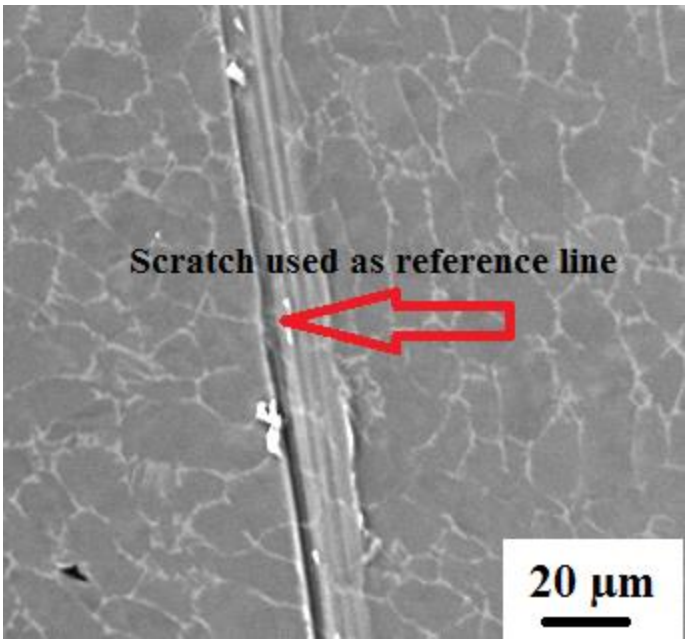

Figure 2.2 SE SEM image of a Ti-8Al-1Mo-1V sample showing the razor blade scratch which was used as a reference line to identify the EBSD scan areas.

EBSD orientation maps were obtained using a field emission Tescan Mira3 SEM, equipped with EDAX-TSL (Mahwah, NJ, USA) EBSD system. The specimens were tilted 70 degrees from horizontal inside the SEM. For the scans, a 25kV electron beam and a working distance of ~20mm was used. The EBSD scans were performed using a step size of 0.5-1 µm, and a 2×2 binning setting was used.

After the EBSD maps were obtained, post-processing "clean-up" was performed using either "Neighbor CI Correlation" or "Grain Dilation" to eliminate erroneous data points arising from un-indexed or inappropriately indexed patterns, . "Neighbor CI Correlation" is done by replacing the orientation of the erroneous data point (generally points with confidence index values <0.1) with the orientation of the neighboring point with the highest confidence index. Grain Dilation is a way for cleaning up data at the boundaries, this method modifies the orientations of the points that do not belong to any grains, and consider them as a single grain. However, for a point or a

group of points must contain some minimum number of data points (5 in the case of a high resolution scan) in order to be considered as a single grain.

2.3 *In-Situ* Mechanical Testing

2.3.1 Sample configuration

For the *in-situ* mechanical testing, flat dog-bone specimens with a 3mm gage width and 10mm length were electrodischarge machined (EDM). Figure 2.3 shows a photograph of an EDM cut specimen. The machined specimens were polished using the method described in section 2.2.1. Table 2.2 lists the testing conditions of the specimens investigated in this study.

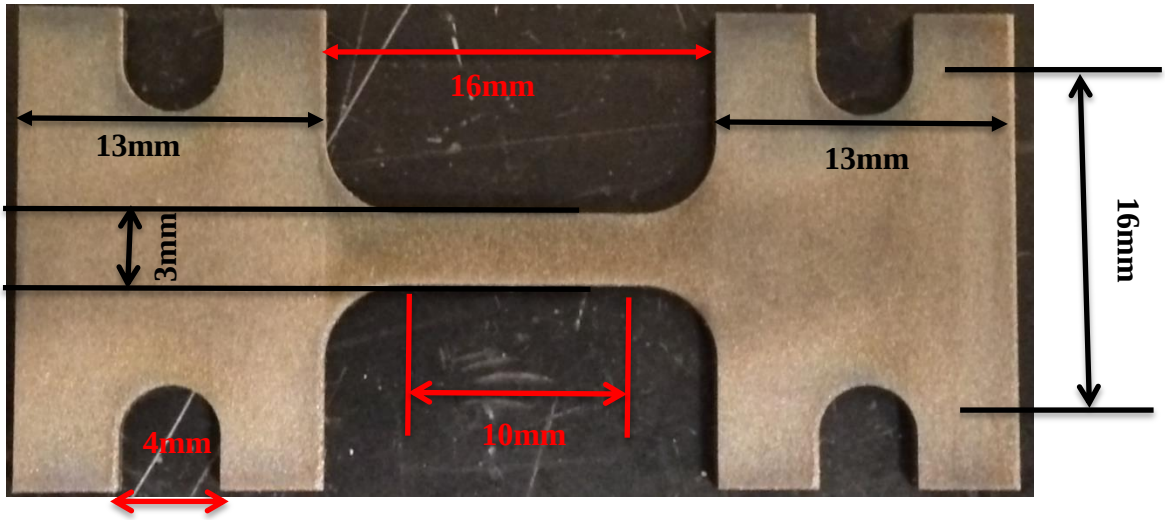

Figure 2.3 A photo of an *in-situ* test specimen representative of those used in the tensile and tensile-creep experiments. The sample dimensions are provided.

Table 2.2 Testing conditions of the investigated specimens (one test was performed per condition).

Test Mode	Temperature
Tension	25^0C (RT)
Tension	260^0C
Tension	455^0C
Tension	650^0C
Tension Creep (440 MPa, ~0.7 yield stress)	370^0C
Tension Creep (315 MPa, ~0.7 yield stress)	455^0C

2.3.2 *In-Situ* Tensile Testing

The *in-situ* tensile tests allow capturing the surface deformation evolution of the specimen with increased stress level at a constant test temperature. A screw-driven tensile stage built by Ernest F. Fullam, Incorporated (originally located in Lantham, NY and later acquired by MTI Instruments, Albany, NY) was inserted inside the Tescan Mira3 SEM. A photo showing the *in-situ* testing setup in the Tescan Mira3 SEM chamber is shown in Figure 2.4.

In-situ tensile tests were performed on the alloy at 25^oC, 260^oC, 455^oC and 650^oC with a constant displacement rate of 0.004 mm/s (i.e. an approximate strain rate of 10^{-3} s^{-1}). The displacement, time, and load data were recorded during the tests using the MTESTW version F 8.8e data acquisition and control software (Admet, Inc., Norwood, MA, USA). SE SEM images were acquired at intervals during the tests by pausing for ~6-7 minutes. Some load relaxation occurred during this time, and the tests were resumed at the same displacement rate after imaging was complete. For the elevated-temperature tensile tests, a 6mm diameter tungsten-based heating unit, powered by a constant voltage power supply, was used to heat the samples to the desired temperature. The desired temperature was maintained for a minimum of 30 minutes before loading. The temperature was monitored using a thermocouple spot-welded to the side of the

gage section. The vacuum was maintained below 2×10^{-6} Torr throughout the experiments. In order to calculate the strain, the relative displacement of two obvious microstructural features was considered.

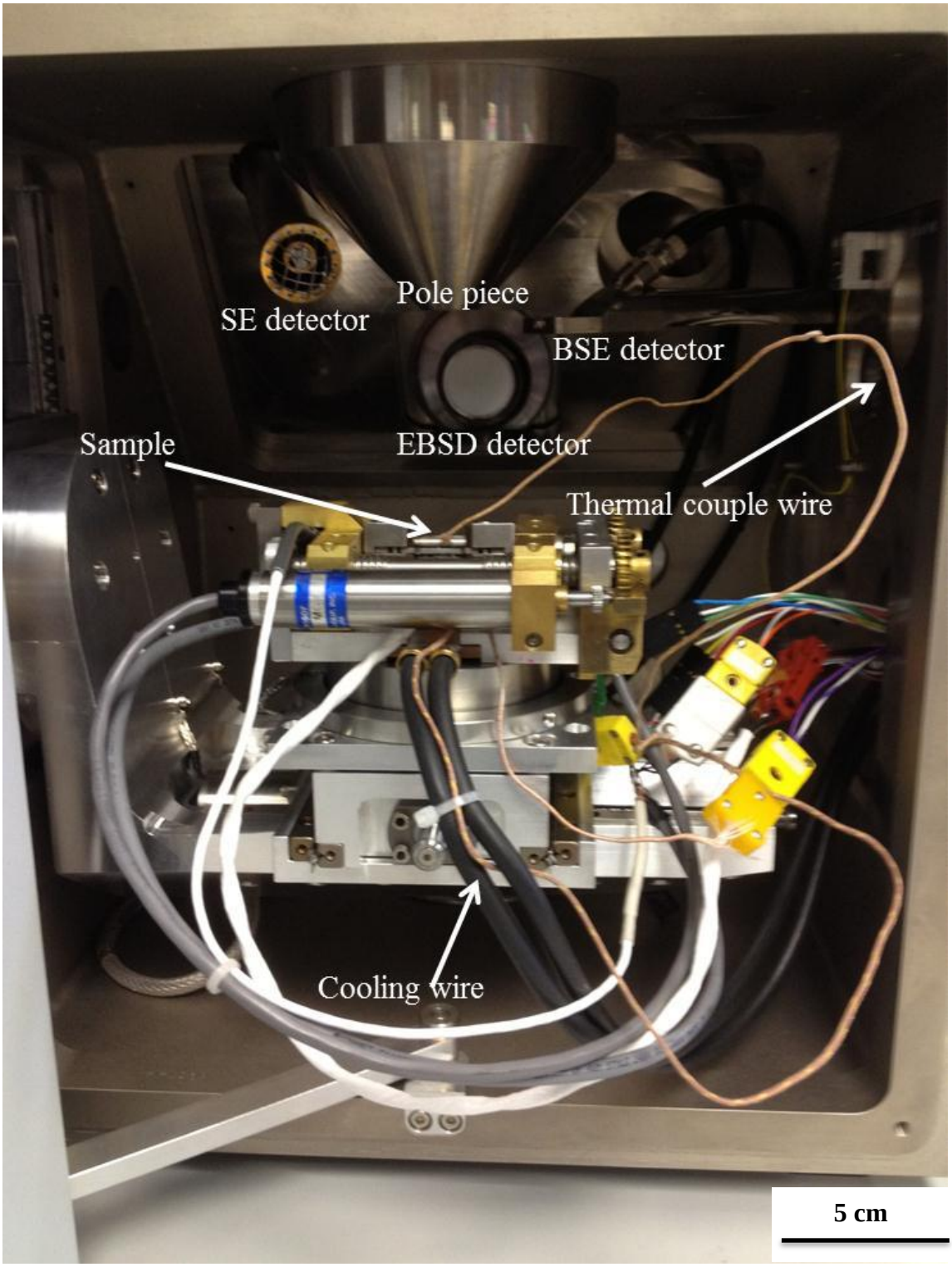

Figure 2.4 A photo showing the *in-situ* testing setup in the Tescan Mira3 SEM chamber.

2.3.3 *In-Situ* Tensile Creep Testing

In-situ tensile-creep experiments were conducted at 370^{o}C-440 MPa and 455^{o}C-315 MPa. In each case the ratio of the applied creep stress versus the YS was in the range of 0.6-0.7. The test set-up was similar to that of the tensile testing, however pausing the experiment for acquisition was not required due to slow deformation during the creep tests. Images were captured at regular intervals to characterize the surface deformation evolution. The temperature was maintained within ±5K of the target temperature for the duration of the experiments. EBSD orientation maps were acquired before starting the experiments.

2.3.4 Slip/Twin Trace Analysis Technique and Schmid factor calculation

A slip/twin trace analysis was used to identify the active deformation systems. Since nearly all of the microstructure consisted of the HCP phase, the slip/twin trace analysis was focused only on the HCP structure. The EBSD analysis provided the crystallographic orientation of each individual grain in the scanned area with reference to the sample/lab coordinate system given by the EBSD data in the form of three Euler angles (φ1, Φ, φ2). The rotation matrix (*g*) between the crystal coordinate system and the sample/lab coordinate system was calculated by:

$$g = \begin{bmatrix} \cos\varphi 2 & \sin\varphi 2 & 0 \\ -\sin\varphi 2 & \cos\varphi 2 & 0 \\ 0 & 0 & 1 \end{bmatrix} \begin{bmatrix} 1 & 0 & 0 \\ 0 & \cos\Phi & \sin\Phi \\ 0 & -\sin\Phi & \cos\Phi \end{bmatrix} \begin{bmatrix} \cos\varphi 1 & \sin\varphi 1 & 0 \\ -\sin\varphi 1 & \cos\varphi 1 & 0 \\ 0 & 0 & 1 \end{bmatrix} \quad (2.1)$$

For a given observed slip trace which is observed, the slip plane and the slip direction can be expressed as (h k l) [u v w] in the crystal coordinate system using Miller indices. The

transformation of the slip plane and the slip direction from the crystal coordinate system to the sample/lab coordinate system can be achieved by (2.2) and (2.3)

$$n = g^T \bullet \begin{bmatrix} h \\ k \\ l \end{bmatrix} \tag{2.2}$$

$$b = g^T \bullet \begin{bmatrix} u \\ v \\ w \end{bmatrix} \tag{2.3}$$

where *n* and *b* are the corresponding slip plane normal and slip direction of a given slip system presented in the sample/lab coordinate system. The plane trace was then calculated by the cross product of the slip/twin plane normal (*n*), expressed in the sample/lab coordinate, and the sample normal direction ([001]). The reason for using the cross product of the slip/twin plane normal and the sample normal to calculate the plane trace is that if slip occurred, the intersection line between the slip/twin plane of a given deformation system and the sample surface should be parallel to the experimentally-observed slip/twin bands. A MatlabTM code [see Appendix, Li 2013] was generated to calculate all the possible plane traces of the deformation systems for a given grain orientation. Identification of the experimentally-observed deformation systems in a given grain were accomplished by comparing the calculated plane traces with the slip plane traces observed in the SE images.

The global Schmid factor (*m*) of each slip/twin system in an individual grain could be calculated by resolving the stress in the slip direction (Burgers vector direction) of a particular slip plane using equation 2.4, assuming uniaxial tension stress state (represented as σ).

$$m = n \bullet \sigma \bullet b^T \tag{2.4}$$

There are three different slip directions on the basal (three <a>) and pyramidal (one <a> and two <c+a>) planes, so the slip direction could not be determined unambiguously by the slip trace. The slip system with the highest Schmid factor was considered as the active slip system when basal or pyramidal plane traces were observed. Also, when the deformation systems exhibited similar plane traces which did not come from the same plane, the deformation system with the highest Schmid factor was chosen.

Figure 2.5 (a) shows a Ti-8Al-1Mo-1V RT tensile-deformed microstructural patch with ~5% local strain, grain no. 275 was one of the grains in that patch. It corresponded to grain no. 275 in the EBSD scan of the same microstructural patch shown in Figure 2.5(b). The Euler angles for that grain were acquired from the EBSD data, and using the MATLAB^{TM} code [Li 2013], the slip traces for all the 24 possible slip systems for the HCP unit cell were generated, as shown in Figure 2.5(d). The experimentally-observed slip trace was compared with the generated slip traces to determine the active slip system in that grain. This process was repeated for all the grains analyzed in the microstructural patch which showed slip traces.

Twinning was not evaluated for the elevated-temperature tensile and tensile-creep tests, since EBSD scans performed on the samples of the elevated-temperature deformed samples yielded a very low overall average CI (<0.1).

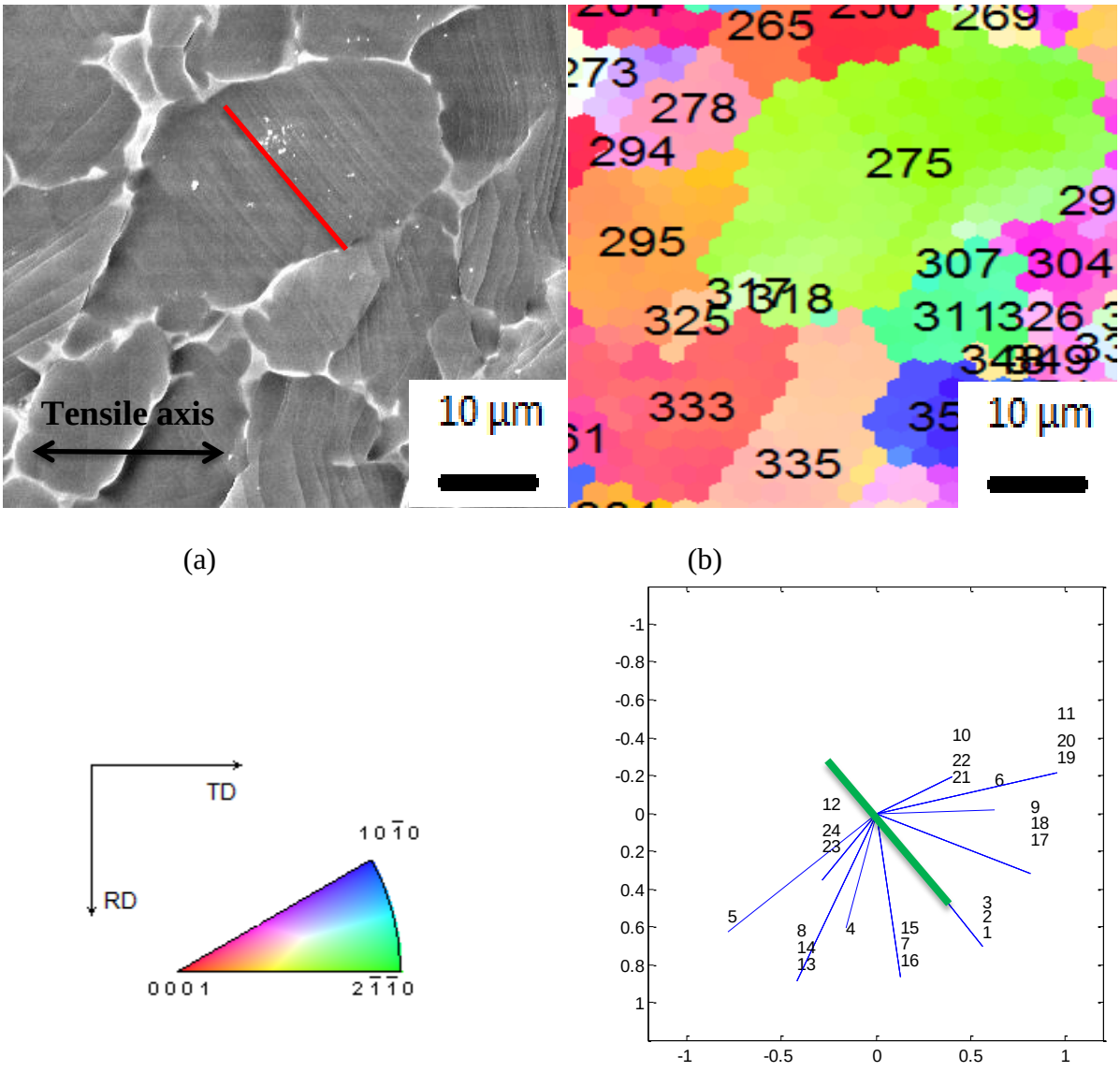

Figure 2.5 Example of slip trace analysis performed on grain 275 in (a), taken for a RT tensile deformed Ti-8Al-1Mo-1V microstructure with ~5% strain. The red line in (a) indicated the experimentally-observed slip band direction. (b) The EBSD IPF map in the tensile direction showing the grain orientation for grain 275. (c) The EBSD color code map and the loading direction. (d) The calculated slip trace directions for all of the possible 24 slip systems and only basal slip systems 1, 2, and 3 matched the experimentally-observed slip band direction. The experimentally-observed slip band direction was indicated by the dark green line. (e) Tabulated slip system chart showing the Schmid factors for all of the 24 slip systems and basal slip system number 3 (0001) [11-20] (bold highlighted in (e)) was determined to be the active slip system with a Schmid factor of 0.49. (f) The HCP unit cell drawing with the calculated slip trace indicated by the red line, the Burgers vector indicated by the light blue line starting from the solid circle, and the slip plane shaded using a gray color.

Figure 2.5 (cont'd)

Slip system number	Slip system type	Slip system	Schmid factor
1	Basal	(0001) [2-1-10]	0.26
2	Basal	(0001) [-12-10]	0.24
3	**Basal**	**(0001) [11-20]**	**0.49**
4	Prismatic	(01-10) [2-1-10]	0.23
5	Prismatic	(10-10) [-12-10]	0.21
6	Prismatic	(-1100) [-1-120]	0.01
7	Pyramidal <a>	(01-11) [2-1-10]	0.32
8	Pyramidal <a>	(10-11) [-12-10]	0.30
9	Pyramidal <a>	(-1101) [-1-120]	0.23
10	Pyramidal <a>	(0-111) [2-1-10]	0.07
11	Pyramidal <a>	(-1011) [-12-10]	0.07
12	Pyramidal <a>	(1-101) [-1-120]	0.25
13	Pyramidal <c+a>	(10-11) [2-1-1-3]	0.35
14	Pyramidal <c+a>	(10-11) [11-2-3]	0.19
15	Pyramidal <c+a>	(01-11) [-12-1-3]	0.19
16	Pyramidal <c+a>	(-1101) [-12-1-3]	0.36
17	Pyramidal <c+a>	(-1101) [-12-13]	0.13
18	Pyramidal <c+a>	(-1101) [-211-3]	0.25
19	Pyramidal <c+a>	(-1011) [-211-3]	0.17
20	Pyramidal <c+a>	(-1011) [-1-12-3]	0.21
21	Pyramidal <c+a>	(0-111) [-1-12-3]	0.19
22	Pyramidal <c+a>	(0-111) [1-21-3]	0.15
23	Pyramidal <c+a>	(1-101) [1-21-3]	0.28
24	Pyramidal <c+a>	(1-101) [2-1-1-3]	0.14

(e)

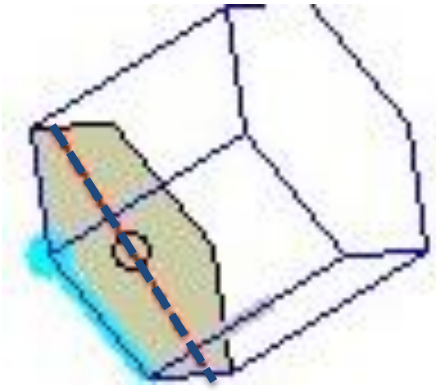

(f)

2.3.5 Method for Estimating CRSS Ratios Of Active Slip Systems

The CRSS ratios of the different deformation modes were estimated using an optimization methodology. The experimentally-observed slip deformation modes in Ti-8Al-1Mo-1V (wt%.) during the tensile and tensile-creep tests (basal <a> slip, prismatic <a> slip, pyramidal <c+a> slip) in all grains from the analyzed microstructural patch were binned based on Schmid factor increments of 0.05, where the values of Schmid factors for each slip system were calculated considering an uniaxial stress state assumption as stated in Section 2.3.4. It is to be noted that CRSS ratios for twinning were not calculated since twinning was not observed during the RT tensile tests, and no twinning was evaluated for the elevated-temperature tensile and tensile-creep tests. Accounting for the texture data, all the possible deformation systems were predicted based on the orientation distribution of all grains in the same microstructural patch, regardless of whether or not the deformation system was activated. For each grain there are 24 possible deformation systems, including 3 basal <a> slip, 3 prismatic <a> slip, 6 pyramidal <a>slip and 12 pyramidal <c+a>slip systems. The distribution of different activated deformation systems in the same microstructural patch was predicted based on the likelihood of deformation system activation as a function of the global Schmid factor, incorporating the distribution of grain orientations in the region of interest. An optimization methodology based on a least-square minimization technique was used to minimize the difference between the experimentally-observed and the predicted number of observations of the different deformation modes. The statistical resampling technique of bootstrapping was used to generate multiple equivalent data sets from which mean CRSS ratios of different deformation systems, with respect to basal slip, was estimated. With statistical analysis, the confidence intervals of the estimated CRSS ratios

were estimated. A MATHEMATICA code [see Appendix, written by Li in 2013] was used to generate the ratios. More details of this methodology can be found in Li *et al.* [2013].

CHAPTER 3

RESULTS AND DISCUSSIONS

3.1 Microstructure

Figure 3.1 shows a representative SE SEM image of the as-received Ti-8Al-1Mo-1V microstructure. The β-phase (body centered cubic structure) was observed along the α-phase (hexagonal close packed structure) grain boundaries, the α-phase consisted of 96±2% of the microstructure. The average α-grain size was 15±3 μm as measured by the line-intercept method [ASTM 2004].

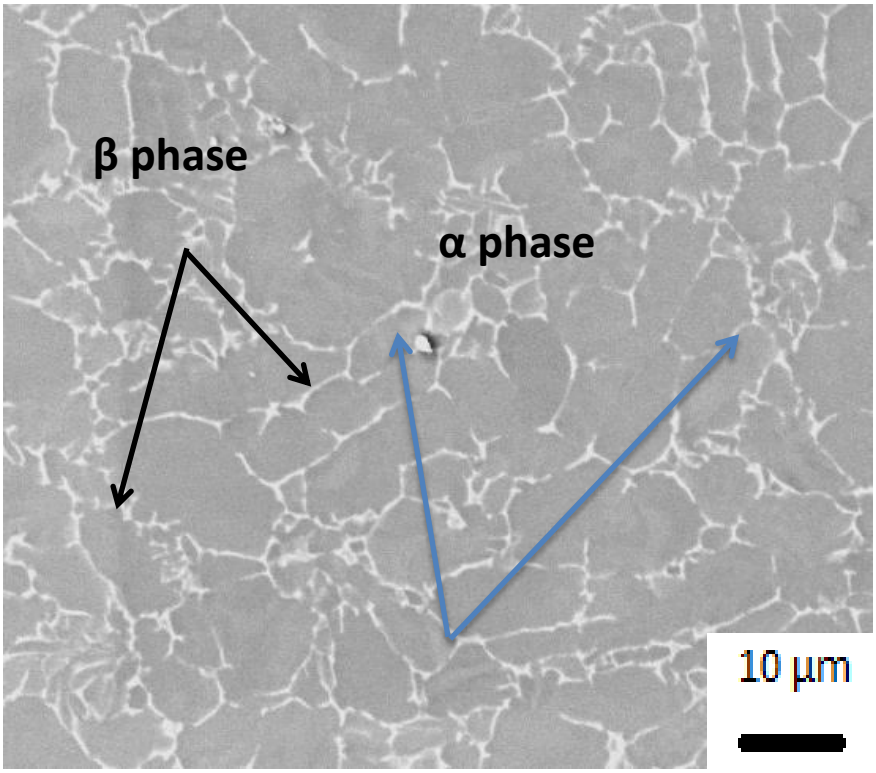

Figure 3.1 SE SEM images showing the microstructure of Ti-8Al-1Mo-1V.

3.2 Texture

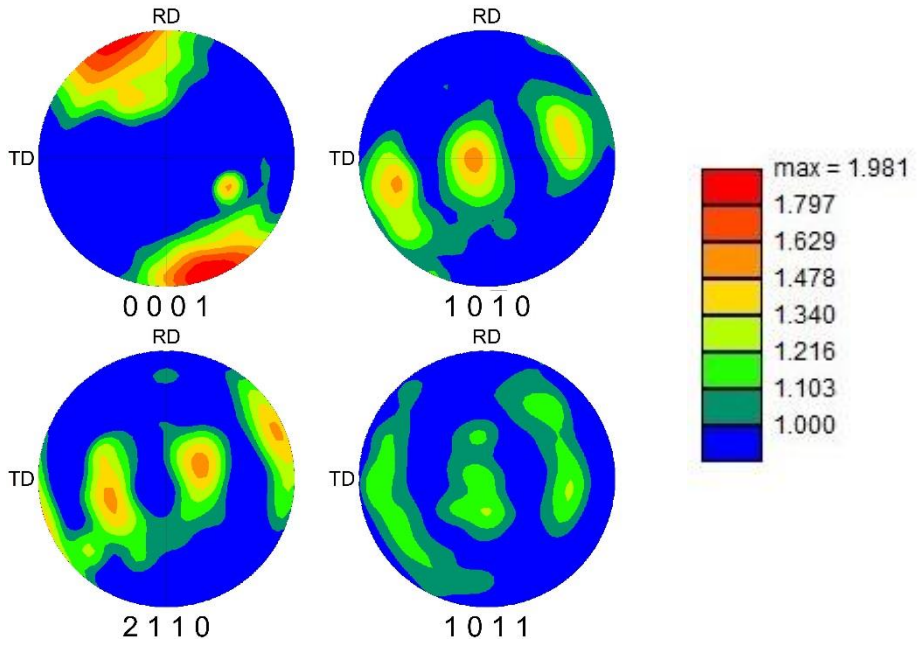

(a)

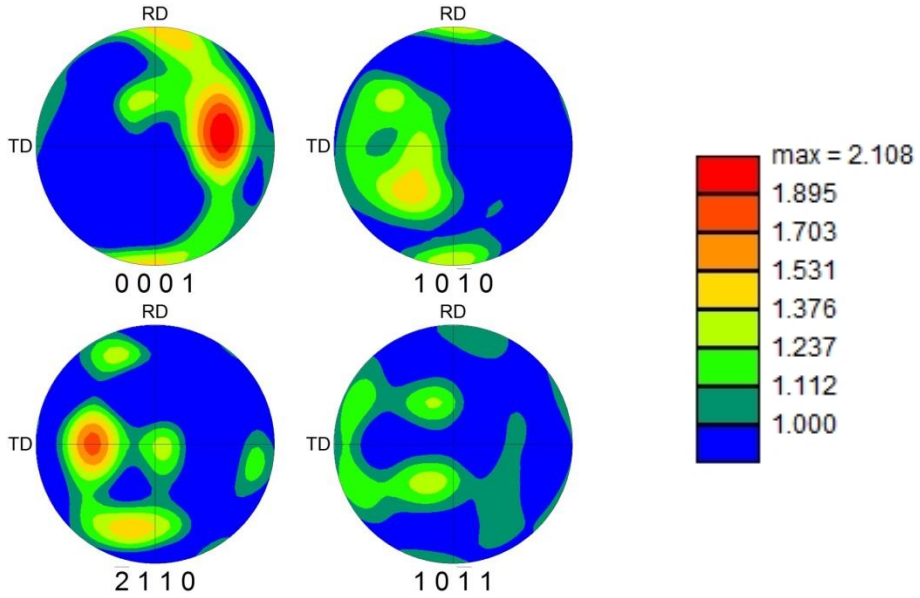

(b)

Figure 3.2: {0001}, {10-10}, {-2110} and {10-11} EBSD pole figure maps from the (a) transverse section (ND || bar axis) and (b) longitudinal section (bar axis being vertical) of the bulk material. (c) {0001}, {10-11} and {11-20} longitudinal EBSD pole figure maps obtained from a selected area of the gage section of a test sample before deformation.

Figure 3.2 (cont'd)

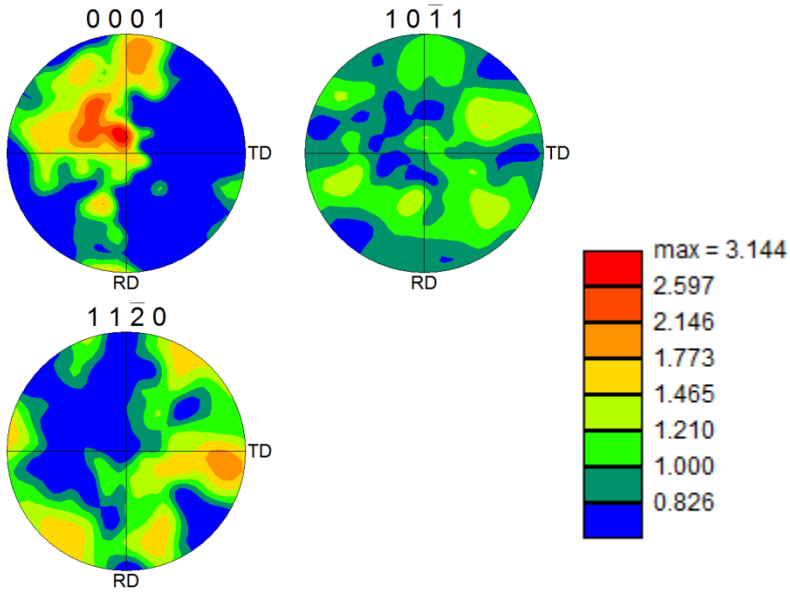

(c)

Figure 3.2 (a) and (b) illustrate the pole figure maps acquired by Dr. Adam Pilchak of Wright Patterson Air Force Base, Ohio, using a step size of 10 µm. Figure 3.2 (c) illustrates the pole figure maps which were extracted from the EBSD data taken from the undeformed test sample. The material possessed a weak texture. The difference in intensities in plots shown in Figure 3(a)-(b) and 3(c) can be explained by the fact that the pole figures acquired by Dr. Pilchak (Figure 3(a)-(b)) are from large EBSD scan areas, which were approximately 30mm x 20mm. However the texture plot shown in Figure 3(c) were obtained from a relatively small selected area on the longitudinal gage section of the specimen, the dimensions of which were approximately 512 µm x 512 µm. These pole figures indicate that the material was not strongly textured.

3.3 Mechanical Behavior

3.3.1 Properties

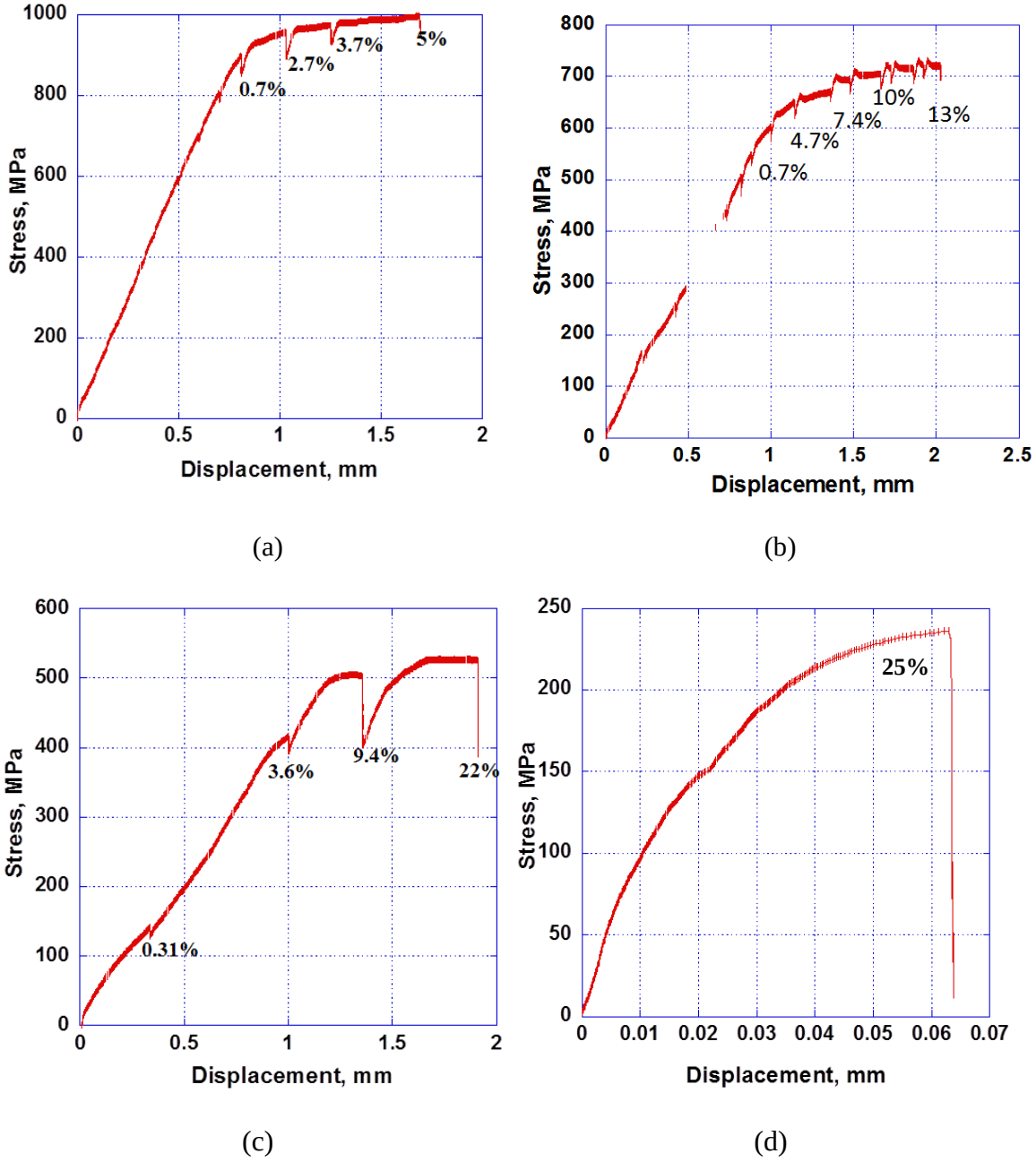

Figure 3.3 Stress vs. displacement plots for Ti-8Al-1Mo-1V samples tested at (a) 25°C, (b) 260°C, (c) 455°C and (d) 650°C. Note that the sample represented in (d) was the only sample that was taken to failure. The stress drops indicate stress relaxation that occurred when the tests were interrupted for capturing the SE images. The local strain values are also indicated on the curve.

The stress vs displacement curves for all the tensile tests performed are shown in Figure 3.3(a)-(d). During the 25°C tensile test, the YS was ~910 MPa, which is consistent with prior studies [Welsch, Boyer and Collings 1993]. The YS dropped to ~650MPa at 260°C. A further drop in YS to ~510 MPa was observed at 455°C. For the 650°C test, the YS was suggested to be 220 MPa.

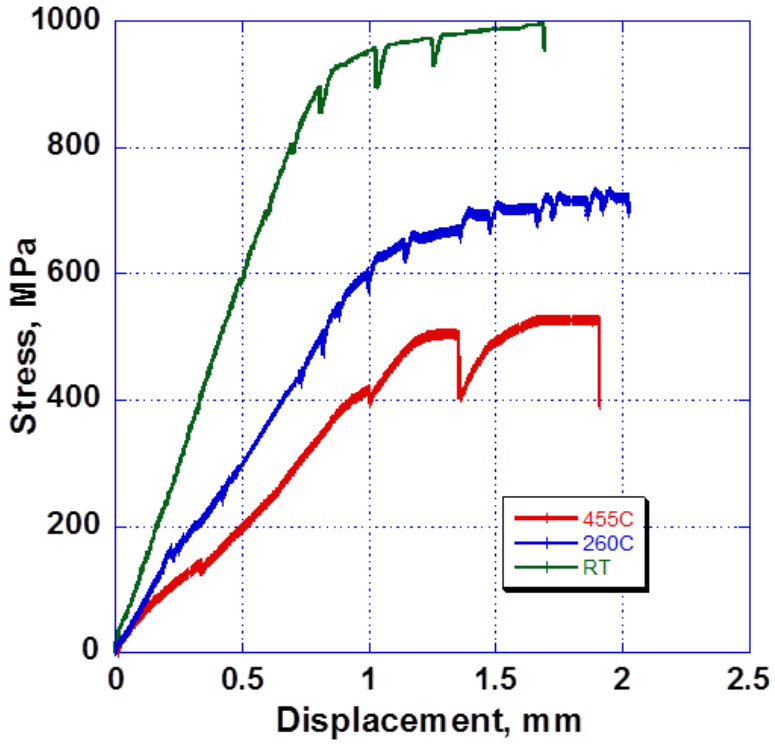

Figure 3.4 Superimposed Stress vs. displacement plots for Ti-8Al-1Mo-1V samples tested at RT, 260°C, 455°C.The load drops indicate relaxation that occurred when the tests were paused for imaging.

The stress vs displacement curves for the tensile tests at 25°C, 260°C and 455°C are shown in Figure 3.4.

The displacement vs time curve for the 370°C-440MPa creep test is shown in figure 3.5.

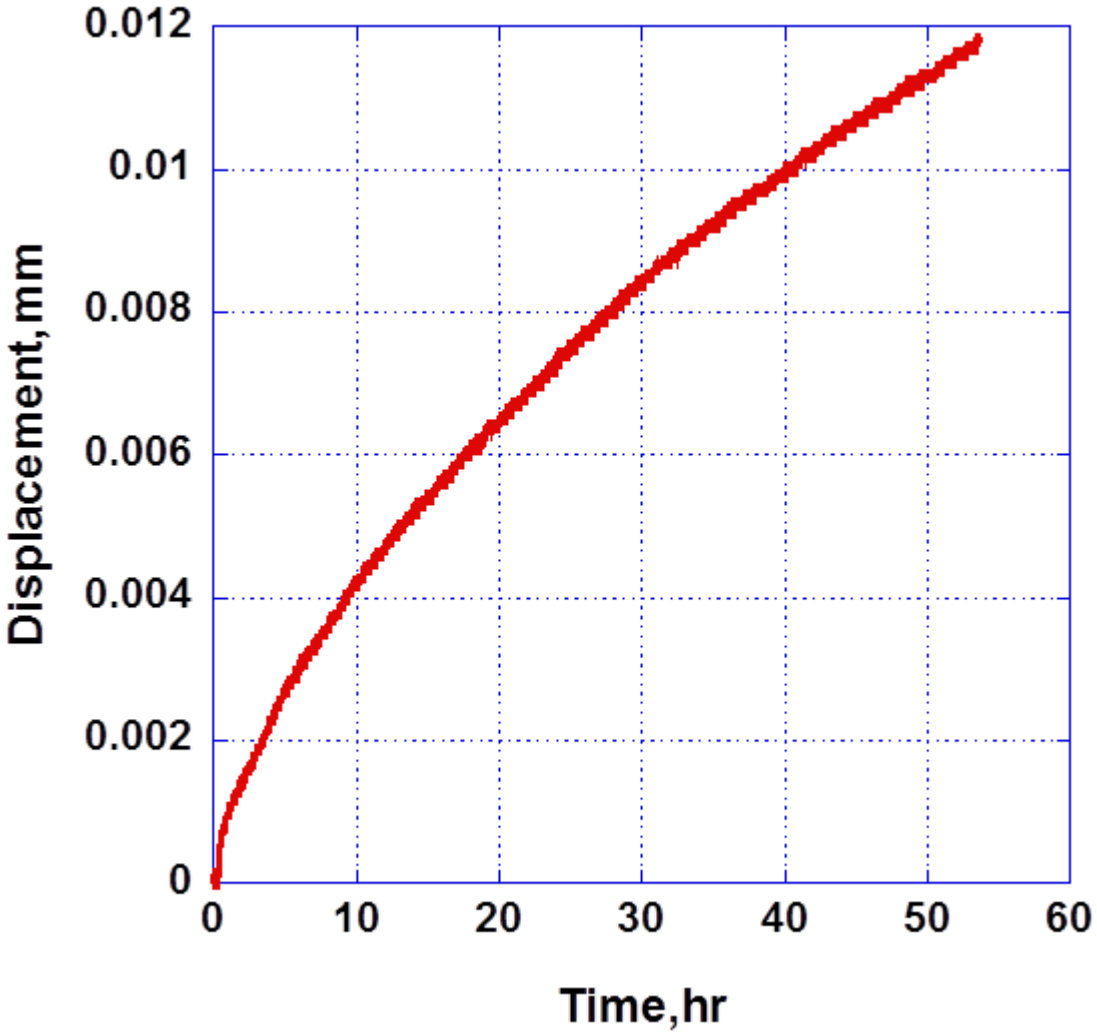

Figure 3.5 Displacement vs. time plot for a Ti-8Al-1Mo-1V sample creep tested at 370°C-440MPa.

3.3.2 Deformation Modes

3.3.2.1 25^{o}C (RT) Tension

During the RT tensile deformation, most of the grains showed evidence of at least one slip trace, while a few grains also showed instances of more than one slip trace. Prismatic slip system was the most frequently observed slip mode. Figure 3.6(a) shows a SE SEM image of the microstructure after ~0.7% strain, and the first instance of slip traces were observed around this strain level. Figure 3.6(b) shows a SE SEM image of the same area of the microstructure at 2.7% strain. According to the stress vs displacement curve, see Figure 3.3a, the sample had already experienced global yielding. More slip traces were observed at higher strain levels. Figure 3.6(c) shows the SE SEM image of the same portion of the microstructure at 3.7% strain. A majority of the grains in the area of interest were observed to exhibit slip traces. The microstructure also indicated a few instances of grain boundary ledge formation .The final strain level achieved was around 5% at a stress level of ~1000 MPa, and the material was not taken to failure. It is noted that no twinning was observed. This was expected based on previous observations of decreased twin activity observed for Ti-Al alloys having larger Al contents [Williams et al. 2002, Li et al. 2012].

(a)

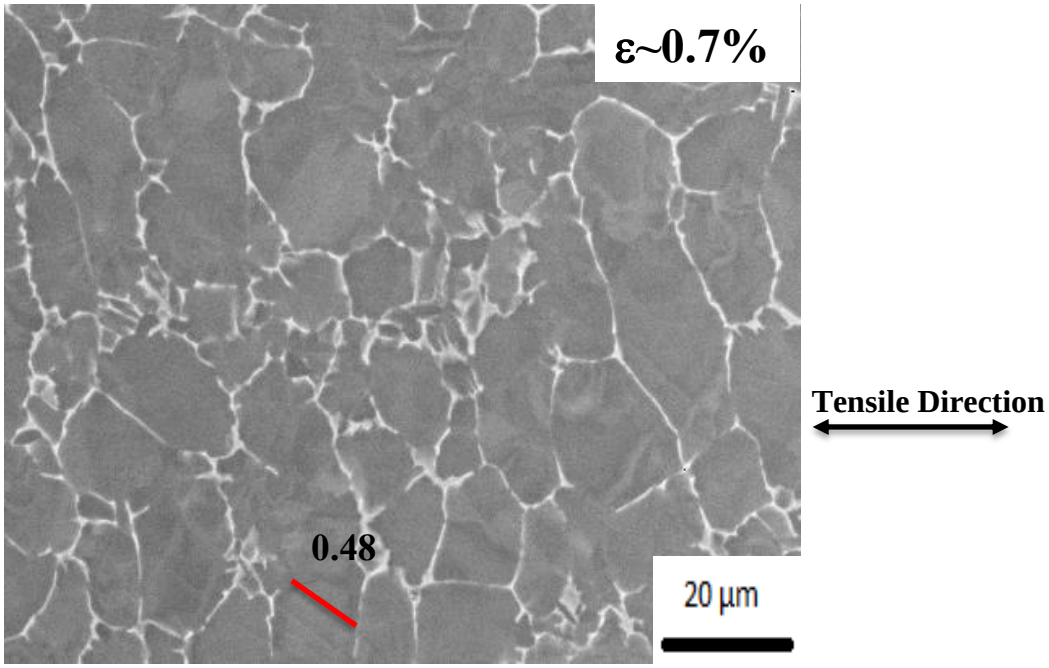

(b)

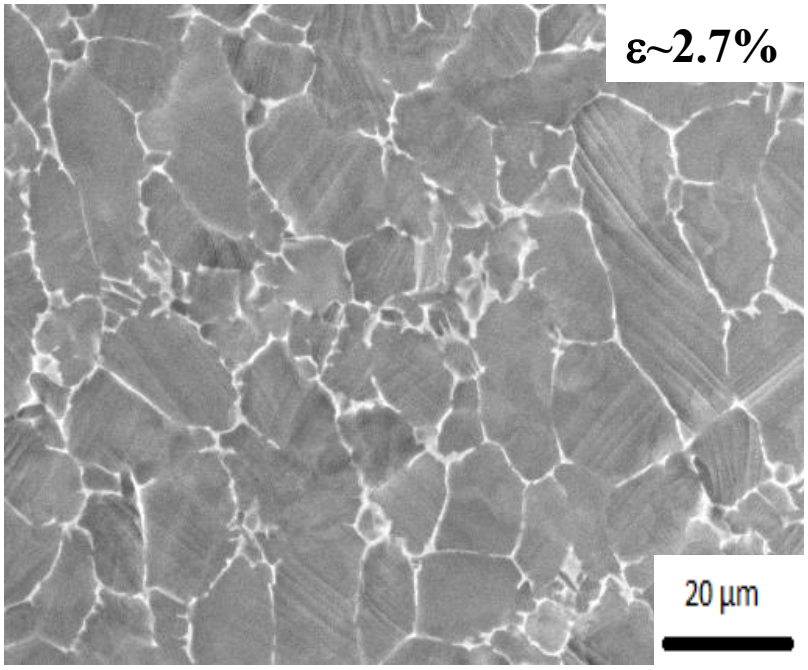

Figure 3.6 Sequential SE SEM images for the Ti-8Al-1Mo-1V RT tensile-tested specimen: (a) 820 MPa (~0.7% strain), when the first slip bands (prismatic slip with a Schmid factor of 0.48) were observed, (b) 920MPa (~2.7 strain) and (c) 950MPa (~3.7% strain). In (a) and (c), some of the traces are color coded for prismatic slip (red), basal slip (green). Some of the associated Schmid factor values are indicated next to the slip traces.

Figure 3.6 (cont'd)

(c)

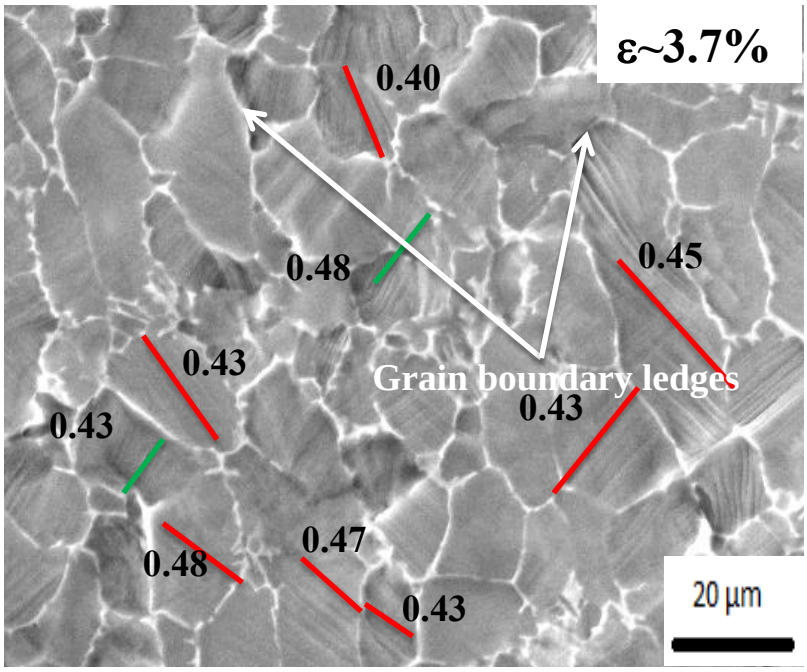

Figure 3.7 illustrates a histogram of the distribution of the slip system activity as a function of the Schmid factor provided in intervals of 0.05, for the RT sample deformed to a strain level of ~3.7%. Prismatic slip accounted for 80% of the total slip system activity and basal slip accounted for nearly 9% of the total slip system activity. In general grains with higher Schmid factors exhibit higher slip frequencies. However, some grains with relatively low Schmid factors (<0.25) exhibited slip traces.

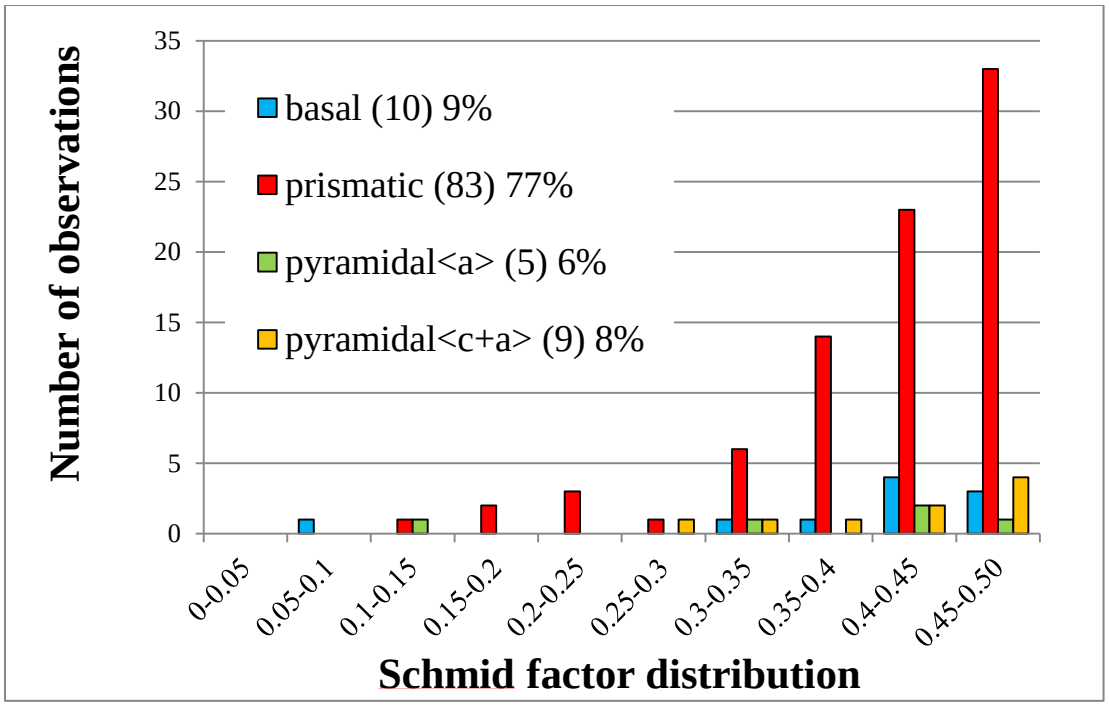

Figure 3.7 A histogram of the Schmid factor distribution of basal, prismatic, pyramidal <a>, and pyramidal <c+a> slip systems for the Ti-8Al-1Mo-1V RT tension sample deformed to ~3.7% strain.

3.3.2.2 260°C Tension

During the 260°C tensile deformation, most of the grains showed evidence of at least one slip trace, while a few grains also showed instances of more than one slip trace. Prismatic slip was still the most frequently observed deformation mode, although the relative amount of basal slip increased compared to prism slip. This suggested that with increased temperature there may be an increase in the relative amount of basal slip activity.

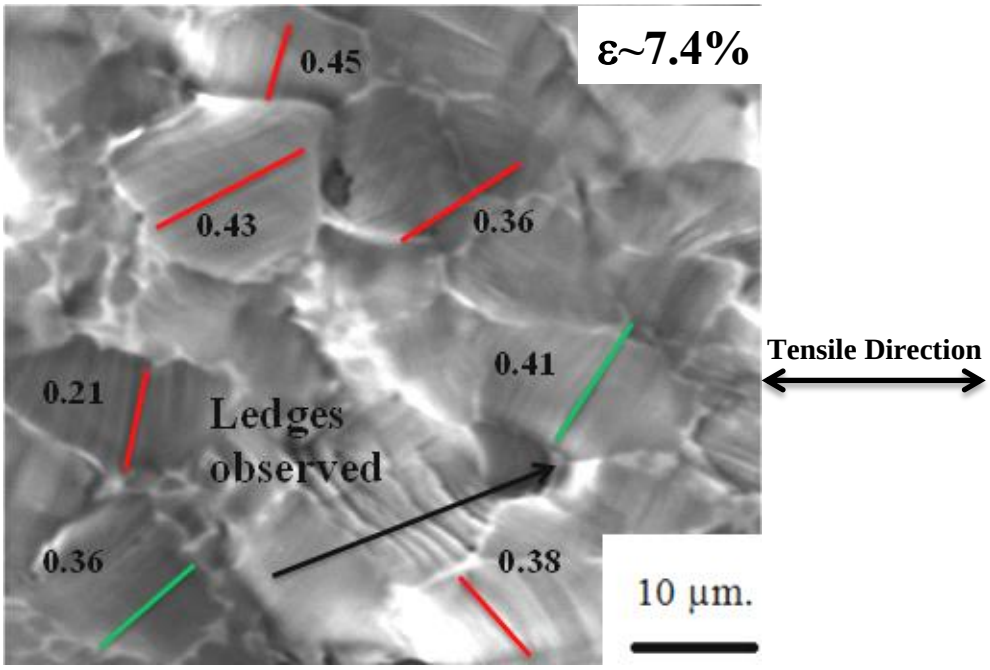

Figure 3.8 SE SEM images for the Ti-8Al-1Mo-1V 260C tensile-tested specimen at 700 MPa(~7.4% strain). The slip are color coded for prismatic slip (red), basal slip (green) and the associated Schmid factor values are indicated next to the slip traces.

In this test, the first slip trace was observed below the global YS. Figure 3.8 shows an SE SEM image of the microstructure during the 260°C tensile test after a deformation of ~7.4% strain. There were instances of wavy slip bands. A few instances of grain boundary ledge formation were also observed and some grain boundary ledges were also observed. The number of grain

boundary ledges was greater than that during the RT tensile test. The final strain level achieved was ~13%

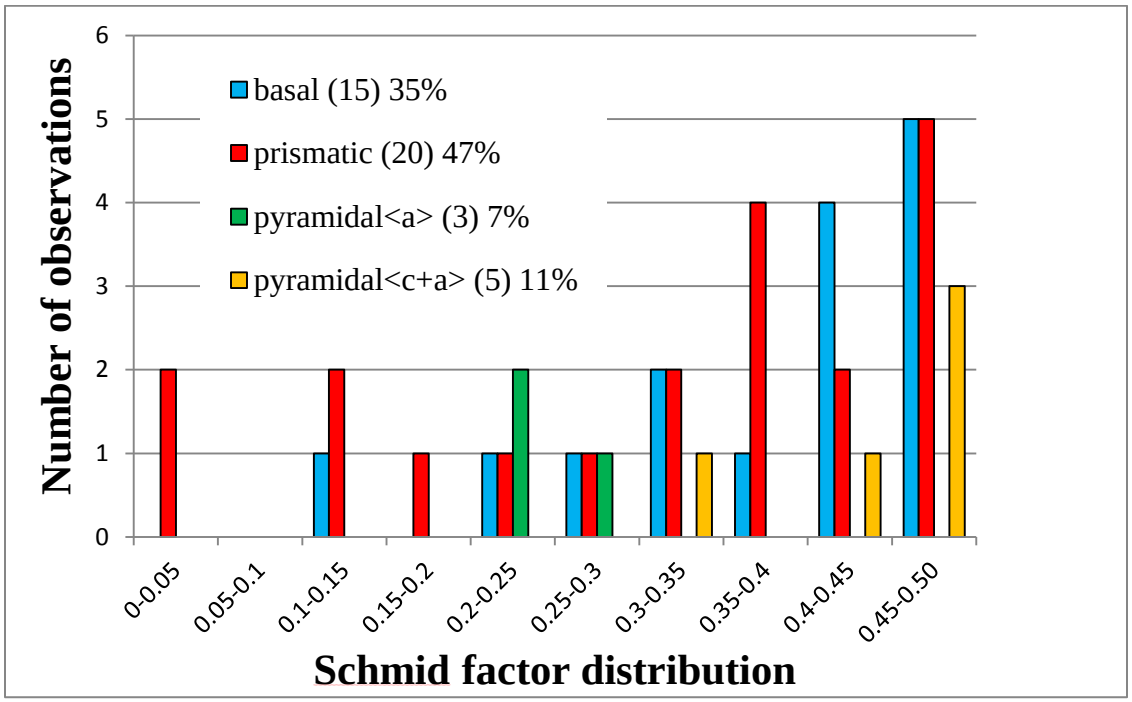

Figure 3.9 A histogram of the Schmid factor distribution of basal, prismatic, pyramidal <a>, and pyramidal <c+a> slip systems for the Ti-8Al-1Mo-1V 260^0C tension experiment after ~7.4% strain.

Figure 3.9 illustrates a histogram of the distribution of the slip system activity as a function of the Schmid factor for the 260^oC deformed sample at a strain level of ~4.8%. Prismatic slip accounted for ~47% of the total slip system activity and basal slip accounted for nearly ~35% of the total slip system activity. No large changes in the relative activation of pyramidal slip activity were observed compared to the RT tensile test. In general, grains with higher Schmid factors exhibited higher slip frequencies. However, some grains with relatively low Schmid factors (<0.25) also showed slip activity.

3.3.2.3 455^{o}C Tension

During the 455^{o}C tensile deformation, most of the grains showed evidence of at least one slip trace, while a few grains also showed instances of more than one slip trace. Basal and Prismatic slip activities were observed in almost equal frequencies. Thus, with increased temperature, the relative amount of basal slip activity increased. The final strain level achieved was ~22 %. Figure 3.10(a) shows an SE SEM image of the microstructure after a deformation of ~3.6% at a stress level of ~405 MPa. This was where the first slip trace was observed. Similar to that observed for the other samples, slip traces were observed prior to yielding. Figure 3.10 (b) shows an SE SEM image of the microstructure at a strain level of ~9.4%, where more slip traces were observed. Some of the earlier observed slip bands were observed to become more prominent. More instances of grain boundary ledges were observed compared to the lower temperature tensile tests. Figure 3.10 (c) showed an SE SEM image of the same area of the microstructure as in at a strain level of 21.4%. This figure shows the first instances of cracking, and cracks developed initiated from the triple point junctions or the grain boundaries.

(a)

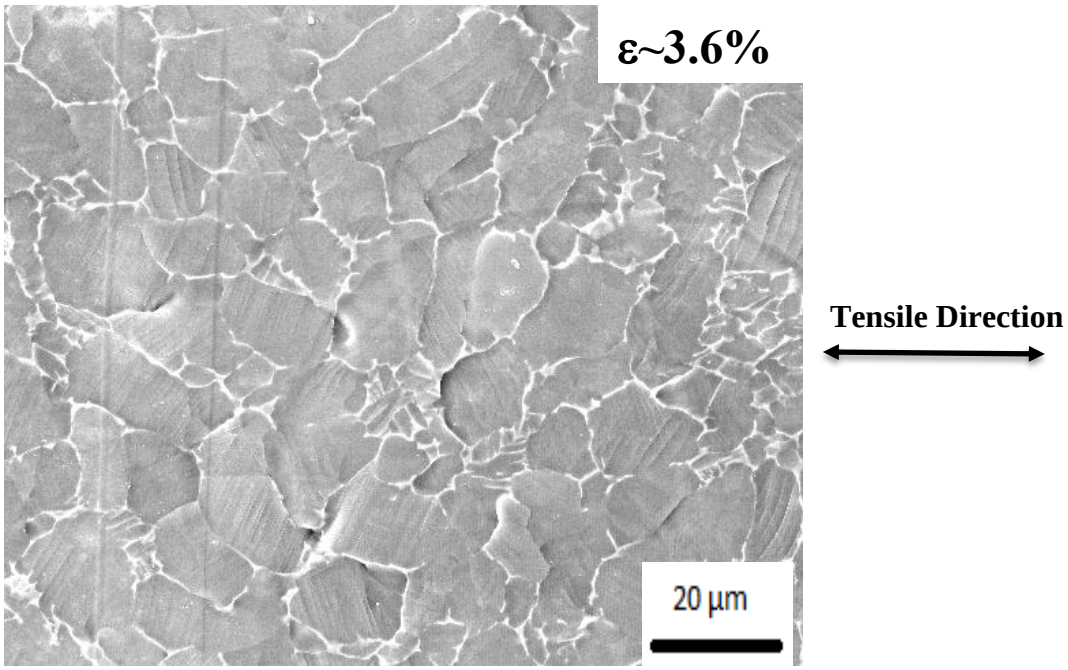

(b)

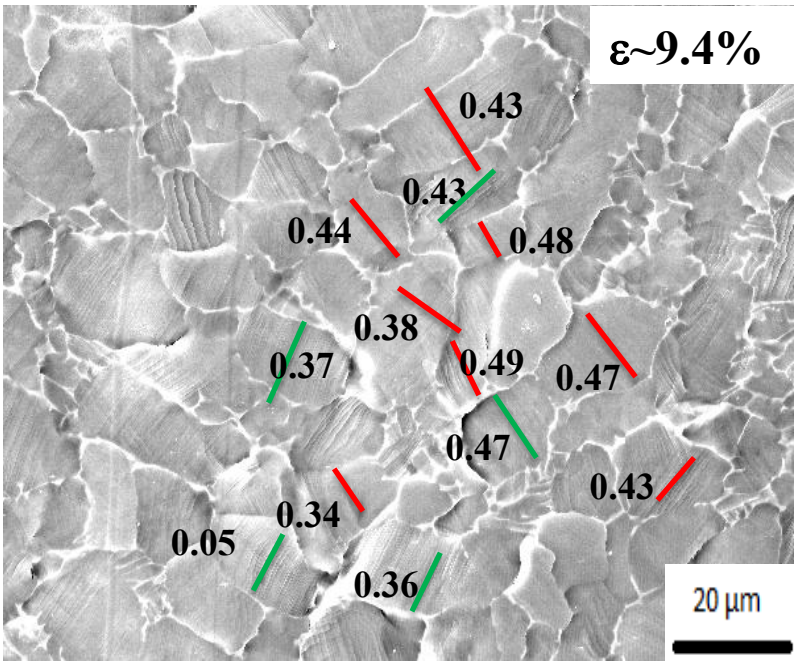

Figure 3.10: Sequential SE SEM images for the Ti-8Al-1Mo-1V 455^{o}C tensile-tested specimen: (a) 405 MPa (~3.6% strain), (b) 448MPa (~9.4 strain) and (c) 458MPa (~21.4% strain). In (b), slip traces are color coded for prismatic slip (red) and basal slip (green), and associated Schmid factors are indicated next to the slip traces.

Figure 3.10 (cont'd)

(c)

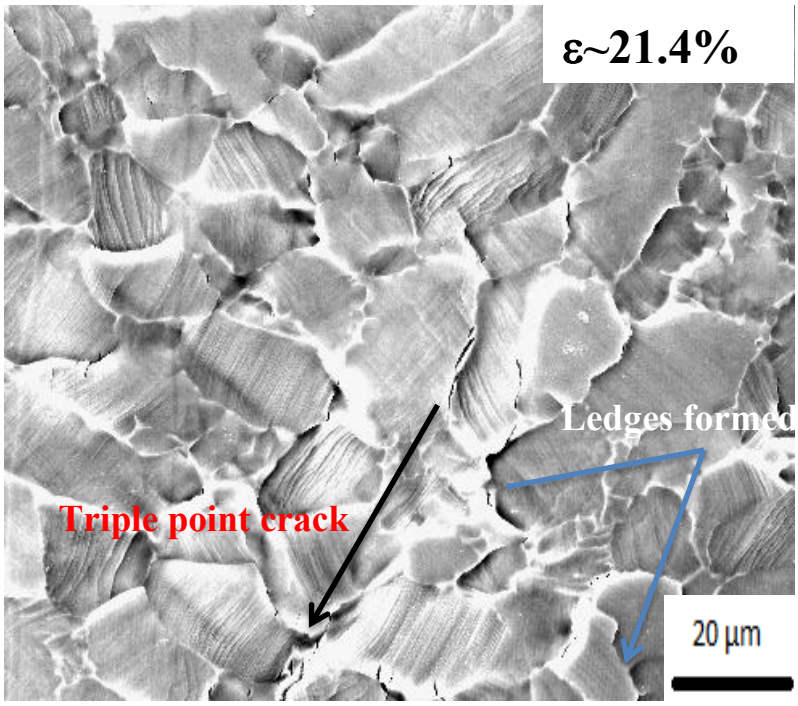

Figure 3.11 illustrates the histogram of the distribution of the slip system activity as a function of the Schmid factor at a strain level of ~9.4%. Prismatic slip accounted for ~40% of the total slip system activity and basal slip activity accounted for ~44% of the total slip system activity. No significant changes in the relative activation of the pyramidal slip system activity were observed compared to the lower temperature tensile test.

Similar to the previously mentioned tests, this histogram also suggested that generally slip systems with higher Schmid factors were activated, although some grains showed slip activity with lower Schmid factors (<0.25).

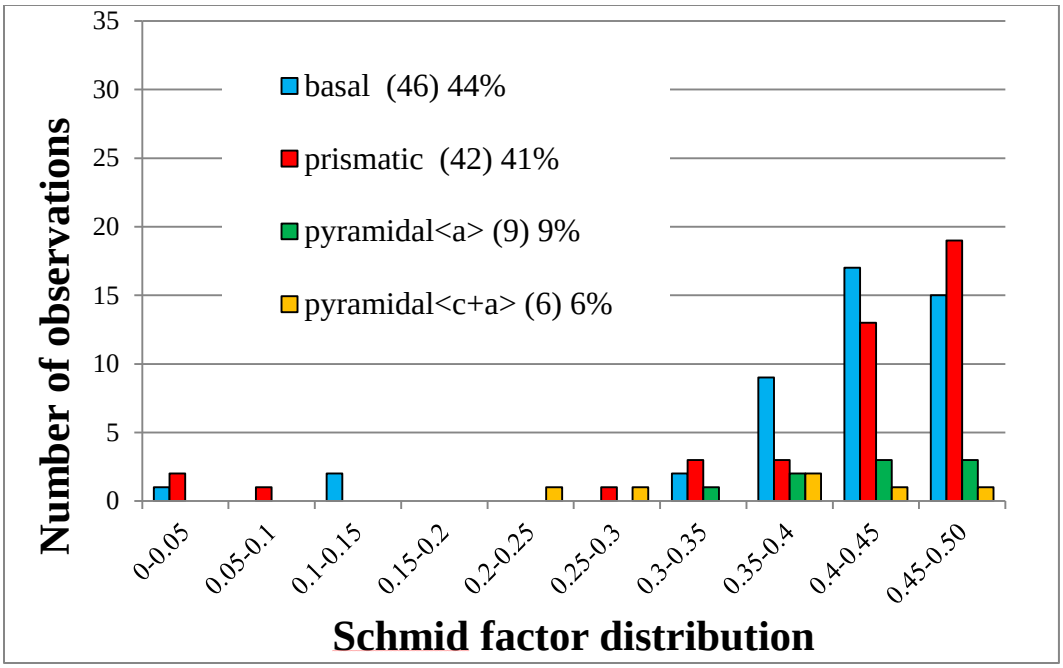

Figure 3.11 A histogram of the Schmid factor distribution of basal, prismatic, pyramidal <a>, and pyramidal <c+a> slip systems for the Ti-8Al-1Mo-1V 455^{0}C tension experiment after ~9.4% strain.

3.3.2.4 650^{o}C Tension

No instances of slip bands were observed during the 650^{o}C tension test, although quite a few instances of grain boundary ledges were observed. The material failed at a stress level of 250 MPa. Surface cracking was observed, and the cracks typically initiated from the triple point junctions or grain boundaries, and later propagated into grain interiors. Figure 3.12 (a) shows an SEM image of the microstructure after failure, which occurred after attaining a strain level of ~25%. No slip traces were observed, however there were more instances of grain boundary ledges compared to the other tensile tests, which suggested that GBS was a likely deformation mode.

The cross-section of the *in-situ* gage section after deformation was metallographically polished to characterize the nature of the cracking. Figure 3.12(a)-(c) show SE images of the cross-section of the gage section of the specimen, and the images showed no evidence of internal cracking which suggested that the cracks observed were localized at the specimen surface. This may have been affected by oxygen diffusion.The diffusivity of oxygen in alpha titanium have been calculated by many researchers. Liu and Welsch [1987] have presented a literature survey on diffusivity of oxygen in alpha titanium which is shown in Table 3.1

Table 3.1 The Pre-Exponential Constants(Do) and Activation Energies(Q) for diffusion of oxygen in Alpha Titanium [Liu and Welsch, 1987]. Serial No. and Ref. are the serial numbers and references used by Liu and Welsch [1987].

Serial No.	Temp (K)	Do (m^2/sec)	Q(kJ/mole)	Alloy	Ref
9	973-1123	5.08 X 10^{-7}	140	Ti	26
13	811-1089	6.20 X 10^{-5}	203	Ti-6Al-2Sn-4Zr-2Mo	22
16	923-1148	4.08 X 10^{-5}	197	Ti	32
23	523-1173	4.50 X 10^{-5}	200±30	Ti	37-41

The diffusivity (D) at a temperature T was caluclated for each of the above four references using the equation (3.1):

$$D = D_o e^{-Q/RT} \quad (3.1)$$

Next the mean diffusion distance was caluclated to estimate the distance the oxygen in the chamber have penetrated during the test. This step was completed using equation (3.2)

$$x = \sqrt{(2Dt)} \quad (3.2)$$

Where "t" is the diffusion time or the time of testing in this case. The time of performing the test was around 1 hr or 3600 secs. This experiment was performed at T=650^{o}C (923K), and the mean diffusion distances for each of the above four set of data are caluclated and shown in table 3.2.

Table 3.2 showing the mean diffusion distance (x) of oxygen in titanium considering the time and temperature mentioned above, for each of the four data sets shown in Figure 3.4. The mean and standard deviation was also calculated.

Serial No.	*x* (µm)	mean	S.D.
9	11.43		
13	2.09	2.63 µm	2.30
16	2.50		
23	2.16		

The diffusion distance at the test temperature and total test time was estimated in the range of 1-3 µm, which is very less compared to the alpha grain size of titanium (~15µm). This suggested that the oxygen in the SEM chamber didn't penetrate deeper and hence only hardened the surface. Oxygen has been reported to have a high solubility in titanium, and therefore the diffusion of oxygen can harden the titanium lattice significantly up to the depth of penetration [Dong et al. 2000]. This makes the surface more hard compared to the interior, and there the surface becomes more resistant to deformation or in other words more brittle. So during the tensile tests, cracks only at the surface were observed due to this oxygen embrittlement, and the cracks opened up perpendicularly to the direction of the tensile axis. The cracks observed during the 455^{o}C tension test can be referred to as surface cracks by the same explanation as above, because the mean diffusion distance will be lower compared to the 650^{o}C tension test.. For the lower temperature, the depth of penetration will be less compared to the elevated temperature tests, and hence less interior will be hardened compared to the higher-temperature test.

(a)

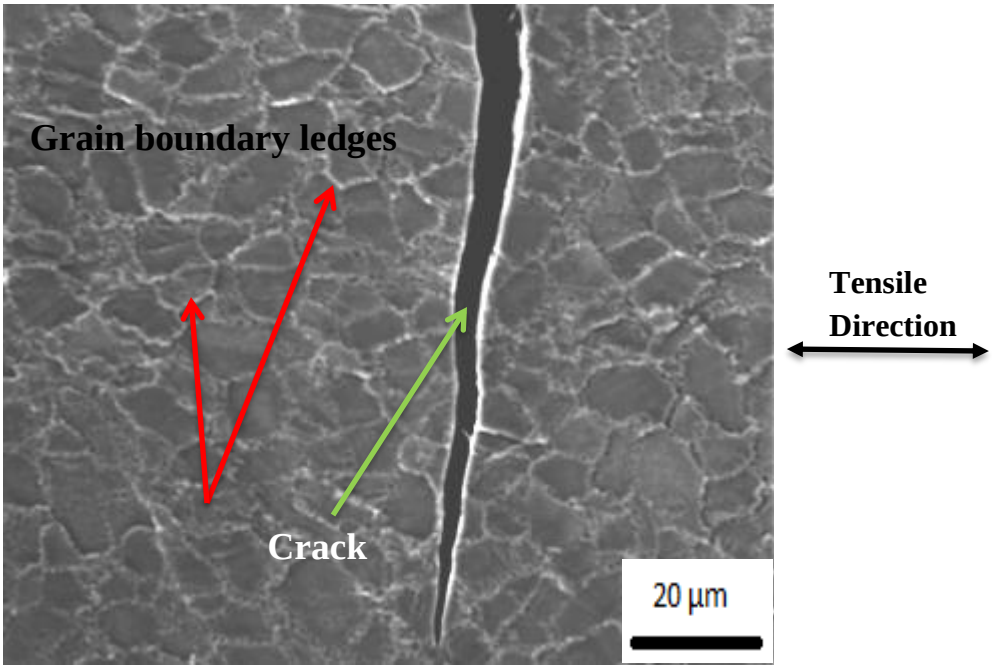

(b)

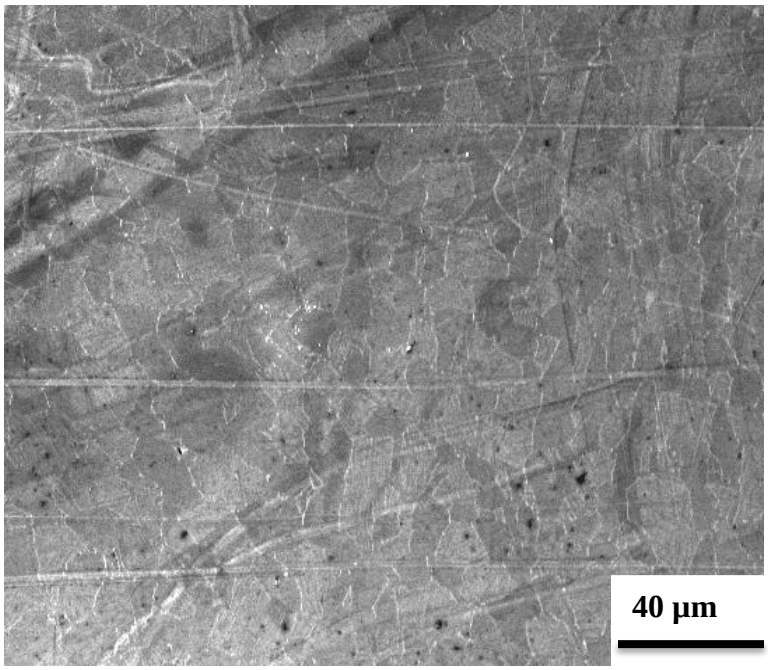

Figure 3.12 SE (a) image of the sample after failure, (b)-(d) Low to High magnification SE images of the polished cross-section of the Ti-8Al-1Mo-1V 650^{o}C tensile tested specimen.

Figure 3.12 (cont'd)

(c)

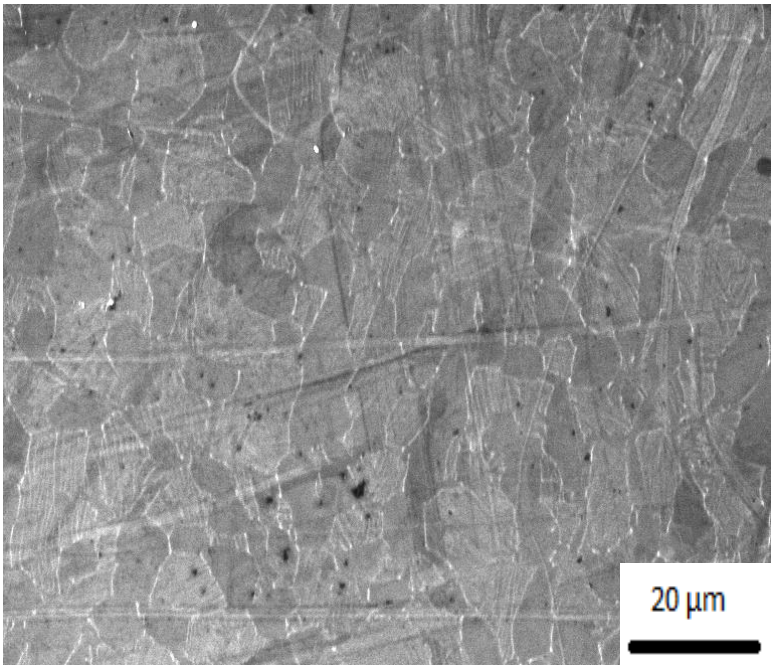

(d)

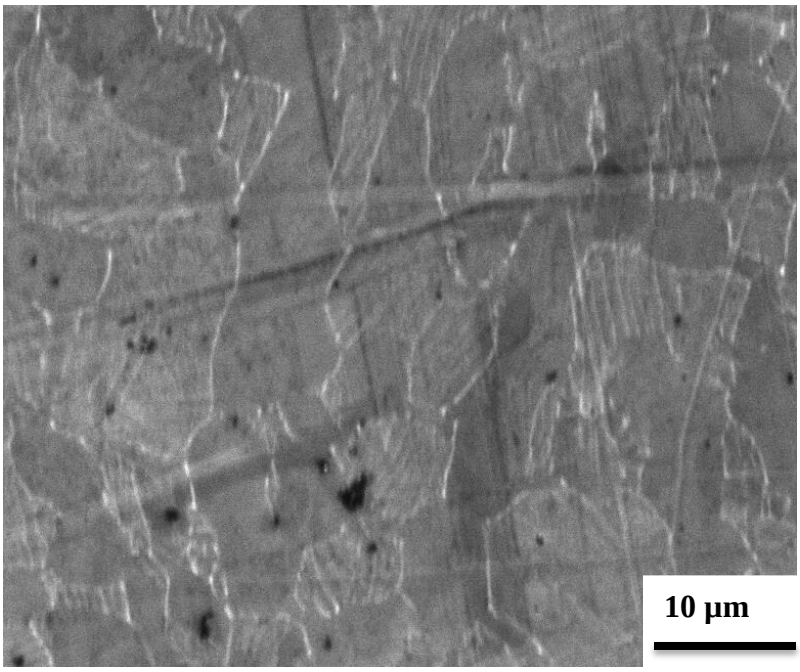

3.3.2.5 370^{o}C-440 MPa Creep

Compared to the tensile tests, a lower percentage of grains showed slip traces in the creep sample deformed at 370^{o}C and 440 MPa. It is noted that based on the tensile data from the literature [Jenkins and Williard 1967] 440 MPa represents ~0.75 of the YS value at 370^{o}C. Like the tensile tests, a few of the grains showed evidences of more than one slip trace. The final strain level achieved was ~9%. Basal slip activity was the most frequently observed slip mode in the grains that exhibited slip traces. Figure 3.13(a) shows an SE SEM image representing a microstructural patch at a strain level of ~5.7%. Grain boundary ledges were prevalent, which suggested that GBS was a likely deformation mode. Figure 3.13(b) shows an SE SEM image of the same microstructural patch at a strain level of ~8.6%. An increase in the number of slip traces was observed along with the development of more grain boundary ledges. Cracks were also observed. The cracks tended to initiate at triple point junctions and grain boundaries.

(a)

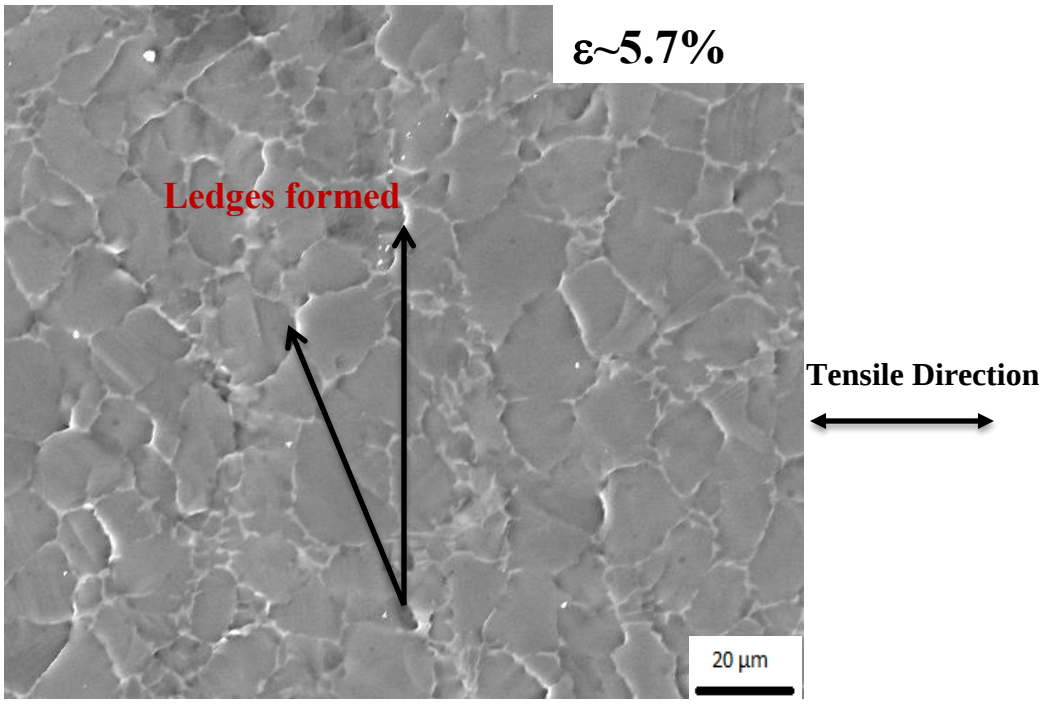

(b)

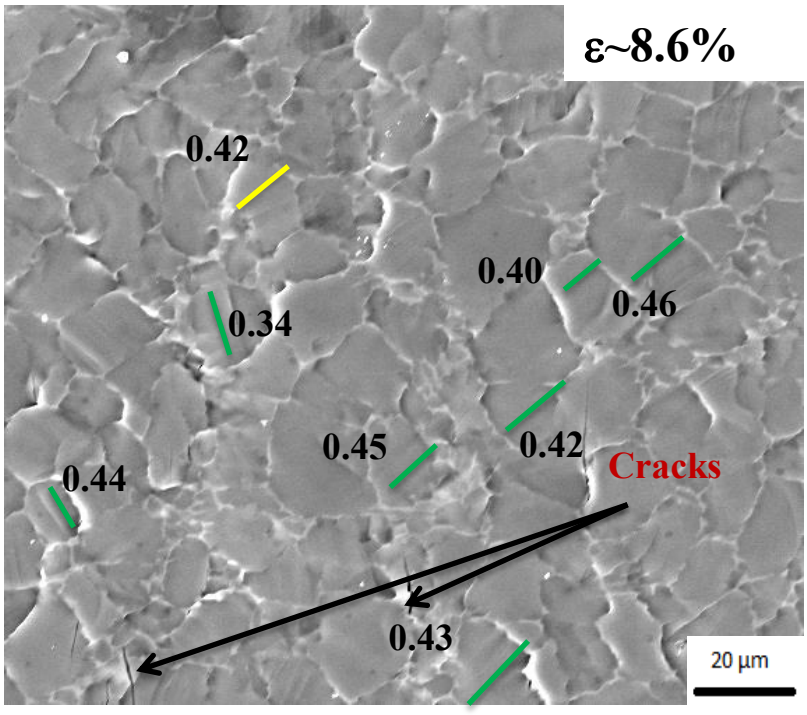

Figure 3.13 Sequential SE SEM images for the Ti-8Al-1Mo-1V 370^{o}C-440 MPa tensile-creep tested specimen: (a) ~5.7% strain, (b) ~8.6 strain. In (b), slip traces are color coded for pyramidal slip (yellow), basal slip (green), and associated Schmid factors are indicated next to the slip traces.

Figure 3.14 shows the histogram of the distribution of the active slip systems in the material as a function of the Schmid factor during the 370°C-440MPa creep test, which showed that basal slip was the dominant deformation mode accounting for 82% of the total slip system activity Pyramidal <c+a> slip activity accounted for 10% of the total slip system activity. Similar to the tensile tests, this histogram also suggested that generally slip systems with higher Schmid factors were more frequently activated, although some grains showed slip activity with lower Schmid factors (<0.25) .

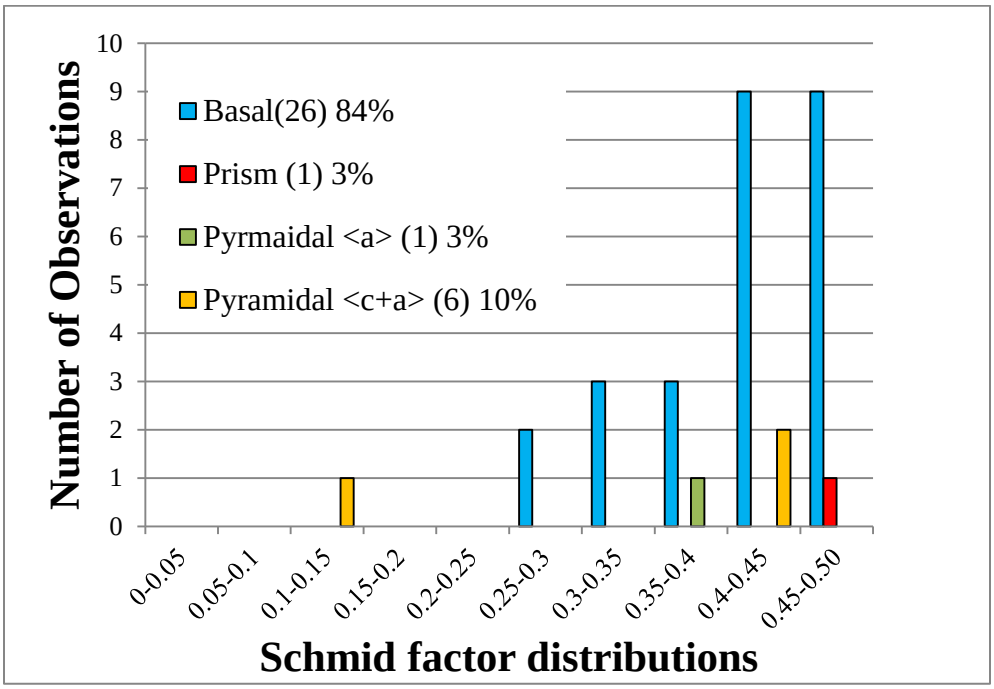

Figure 3.14 A histogram of the Schmid factor distribution of basal, prismatic, pyramidal <a>, and pyramidal <c+a> slip systems for the Ti-8Al-1Mo-1V 370°C-440MPa tension-creep experiment after ~8.6% strain.

Cracks which originated during the 370°C-440 MPa creep test, were also localized to the specimen surface.

The cracks observed during this test in the were characterized using slip trace analysis to determine the plane they were formed on.

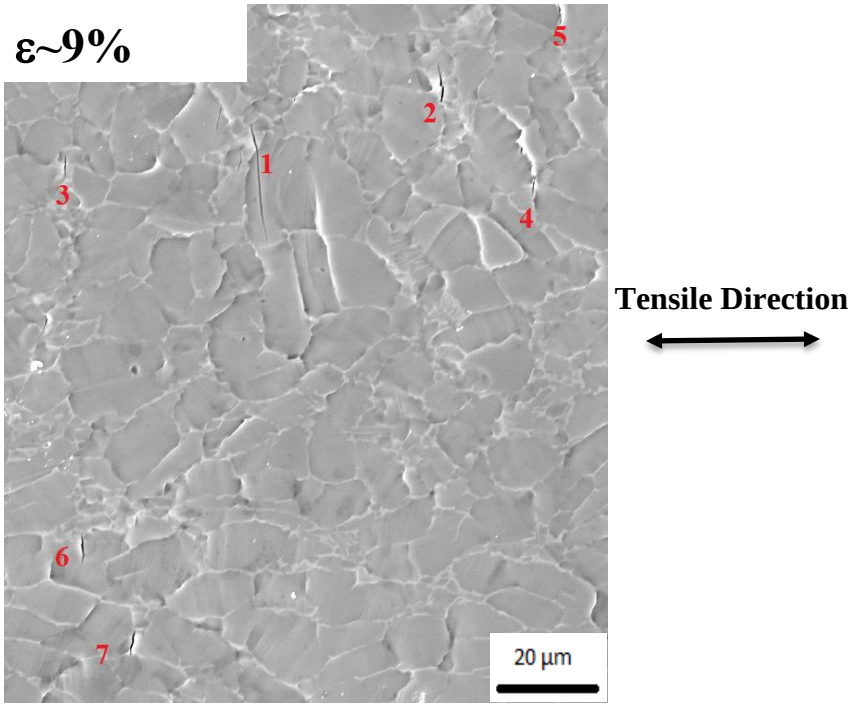

Figure 3.15 SE SEM images for the Ti-8Al-1Mo-1V 370^{o}C-440 MPa tensile-creep tested specimen showing instances of cracking (~9% strain). The cracks observed here are numbered 1-7 were characterized using surface slip trace analysis.

Of the seven cracks shown in Figure 3.15, all have been characterized to from on the basal planes. This suggests that the basal plane is the most susceptible to cracking during this creep test condition for this alloy.

3.3.2.6 455^{o}C-315 MPa Creep

A stress level of 315 MPa represents 0.6 of the YS value at 455^{o}C. Like the previous creep test, a lower number of grains showed evidence of slip traces compared to the tensile tests. In the grains that exhibited at least one slip trace, basal slip activity was again the most frequently observed slip mode. However an increased frequency of prismatic slip activity was observed. This suggests that the test condition (i.e. stress and temperature) could have an effect on the relative deformation mode activity. The final strain level achieved was ~5%. It is noted that this test was stopped while the sample had only achieved 5% strain, which is less than that for the previous creep specimen, which achieved 9% strain.

Figure 3.16(a) shows an SE SEM image which represents the microstructural patch of the sample creep deformed at 455^{o}C-315MPa at strain level ~3%. Grain boundary ledges were prevalent, which suggested that GBS was a likely deformation mechanism. Figure 3.16(b) shows an SE SEM image of the same microstructural patch area at a strain level of ~4%. The only changes observed were further deepening of slip bands. The number of observed slip traces increased with increasing strain level. Cracking was observed.

(a)

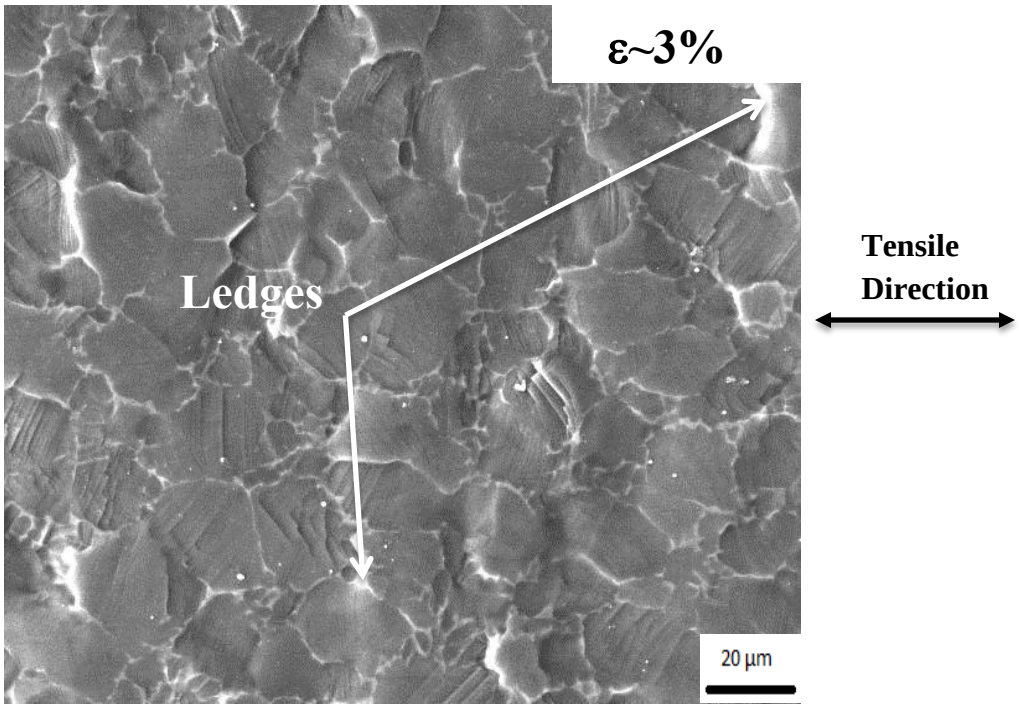

(b)

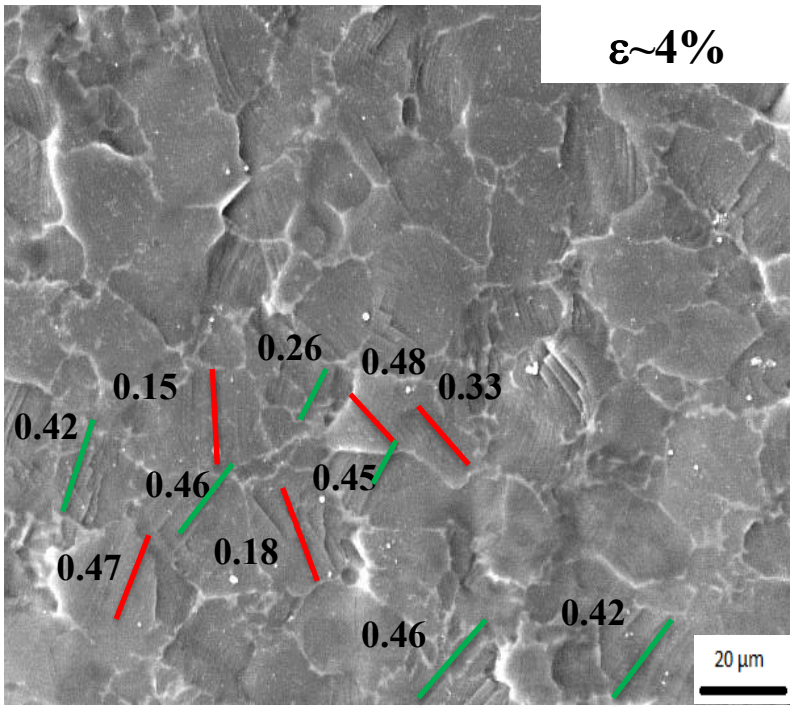

Figure 3.16 Sequential SE SEM images for the Ti-8Al-1Mo-1V 455^{o}C-315 MPa tensile-creep tested specimen: (a) ~3% strain, (b) ~4% strain. In (b), slip traces are color coded for prismatic slip (red), basal slip (green), and associated Schmid factors are indicated next to the slip traces.

Figure 3.17 shows a histogram showing the distribution of the active slip systems as a function of the Schmid factor during the 455°C-315 MPa creep test after a deformation level of ~4%. Basal slip activity accounted for ~44% of the total slip system activity. Prismatic slip system activity accounted for ~38% of the total slip system activity. Compared to the 370°C 440MPa creep test, the relative pyramidal <a> slip system activity increased.

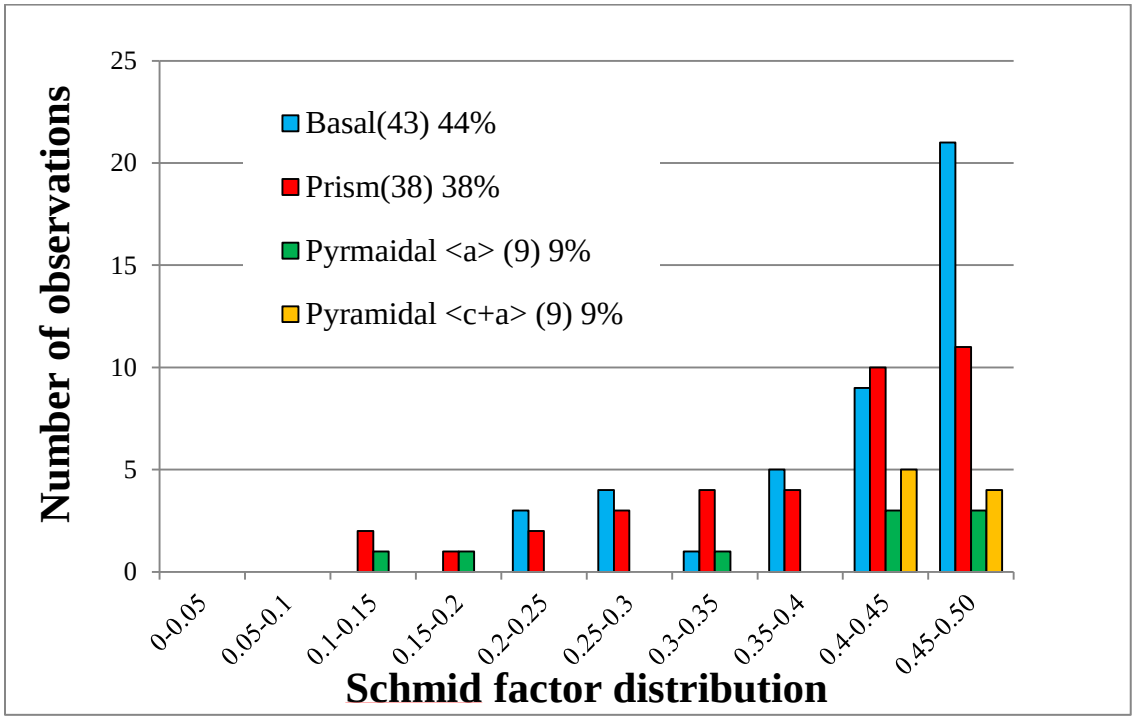

Figure 3.17 A histogram of the Schmid factor distribution of basal, prismatic, pyramidal <a>, and pyramidal <c+a> slip systems for the Ti-8Al-1Mo-1V 455^{0}C-315MPa tension-creep experiment after ~4% strain.

Similar to the tensile tests, this histogram also suggested that slip systems with higher Schmid factors were more frequently activated, although some grains showed slip activity with lower Schmid factor (<0.25).

3.3.2.7 Discussions

Table 3.3 Deformation Summary of Tested Specimens.

Test condition	Number of grains analyzed	(%) of grains showing slip traces	Deformation mode	
			Dislocation Slip	Grain boundary ledge/ sliding
RT tension	117	~92	10% basal, 77% prismatic	not prevalent
260^{o}C tension	46	~93	35% basal, 47% prismatic	not prevalent
455^{o}C tension	109	~94	44% basal, 41% prismatic	not prevalent
370^{o}C, 440 MPa creep	162	~21	84% basal, 3% prismatic	prevalent
455^{o}C, 315 MPa creep	138	~72	44% basal, 38% prismatic	prevalent

Table 3.3 summarizes the deformation of the tested specimens. The deformation mechanisms were dependent on the test conditions. During the tensile tests, dislocation slip was prevalent. Prismatic slip activity was prevalent during the RT tensile testing. With increased temperature, basal slip activity became more prevalent. At 455^{o} an almost equal number of basal and prismatic slip activities were observed. Compared to the tensile tests, the creep samples exhibited a lower number of grains which exhibited slip traces at similar strain levels. This is consistent with the work of Li *et al.* [2012]. This could be due to the level of applied stress which was ~0.6-0.8 of the YS. Since dislocation slip is generally favored at high stress level (Lüthy et al. 1979), one would expect less slip traces during the creep experiments. Basal slip activity was the dominant slip activity observed in both the creep tests, although there was a change in the relative amount of the prismatic slip activity observed between the two tests. This is consistent with the idea that both stress and temperature play an important role in determining the slip system activities in Ti alloys (Li et al. 2012). During the 650^{o}C tensile test, only grain boundary ledges were observed, suggesting GBS to be a likely deformation mode during that test. There were an increased number of grain boundary ledges during the creep tests, which suggested that GBS was a likely deformation mode during the creep tests. The cracks observed during the low

temperature-high stress creep test initiated from the grain boundaries and from the triple point junctions. The cracks developed during the tensile and tensile-creep tests were suggested to be surface cracks which originated due to the diffusion of oxygen inside the SEM chamber into the specimen surface. The high temperature-low stress creep test was a relatively short test. This could be a potential reason why cracking was not observed in that test. The cracks observed during the 370^{o}C-440 MPa test were formed on the basal planes.

3.4 Estimation of CRSS Ratios for the Active Slip Systems

The resulting CRSS ratios of the different slip deformation systems during all the tensile and tensile-creep tests for Ti-8Al-1Mo-1V are shown in Table 3.4 and Table 3.5.

3.4.1 Estimation of CRSS ratios before and after statistical bootstrapping

Table 3.4: Estimated CRSS ratios of the four different slip systems observed in Ti-8Al-1Mo-1V during all the experiments conducted (before performing bootstrapping analysis).

Test	Strain	Basal	Prism	Pyramidal<a>	Pyramidal<c+a>
Tensile (RT)	~3.7%	1	0.32	10.19	6.11
Tensile (260^{o}C)	~7.4%	1	0.66	20.40	7.88
Tensile (455^{o}C)	~9.4%	1	1.06	9.39	44.23
Tensile Creep (370^{o}C-440MPa)	~8.6%	1	7.50	31.63	37.19
Tensile Creep (455 ^{o}C-315MPa)	~4.0%	1	1.37	11.59	13.68

Table 3.5: Estimated CRSS ratios of the four different slip systems observed in Ti-8Al-1Mo-1V along with means and standard errors (the numbers in brackets) respectively, during all the experiments conducted (after performing bootstrapping analysis).

Test	Strain (%)	Prism / Basal	Pyramidal <a> / Basal	Pyramidal <c+a> / Basal
Tensile (RT)	~3.7	0.20	10.07	4.24
		(0.32,0.12)	(45.17,283.24)	(7.31,4.52)
Tensile (260^{o}C)	~7.4	0.41	29.56	3.28
		(0.73,0.37)	(27.06,19.78)	(10.52,8.72)
Tensile (455^{o}C)	~9.4	1.03	10.46	46.22
		(1.09,0.26)	(10.92,7.51)	(65.43,106.46)
Tensile Creep (370^{o}C-440MPa)	~8.6	Bootstrapping was not successful, could be due to the relatively less number of observations (see Table 3.3)		
Tensile Creep (455 ^{o}C-315MPa)	~4	1.73	10.78	11.64
		(1.42,0.38)	(14.74,28.29)	(15.58,8.28)

Comparison of the CRSS ratios before and after bootstrapping shows some changes in the CRSS ratios under all conditions, and this could possibly be due to high convergence of the data obtained after bootstrapping. The CRSS values that were obtained after the bootstrapping, analysis were considered for the rest of this thesis unless otherwise mentioned.

3.4.2 Comparison of CRSS ratios under different conditions

During the tensile tests it can be observed from Table 3.5 and Figure 3.18 that with increased temperature the CRSS ratio for prism: basal slip also increases. Thus basal slip activity becomes more prevalent at higher temperature. This is consistent with Williams *et al.* [2002] who has suggested that basal slip becomes more dominant with higher-temperature deformation. Hence, the CRSS value for basal slip decreases with temperature.

The CRSS ratios for pyramidal<a>: basal slip and pyramidal<c+a>: basal slip first increased and then decreased with temperature, and the reason is not clearly understood. Zeng *et al.* [2009] suggested that at elevated temperatures there are more chances of pyramidal <c+a> slip.

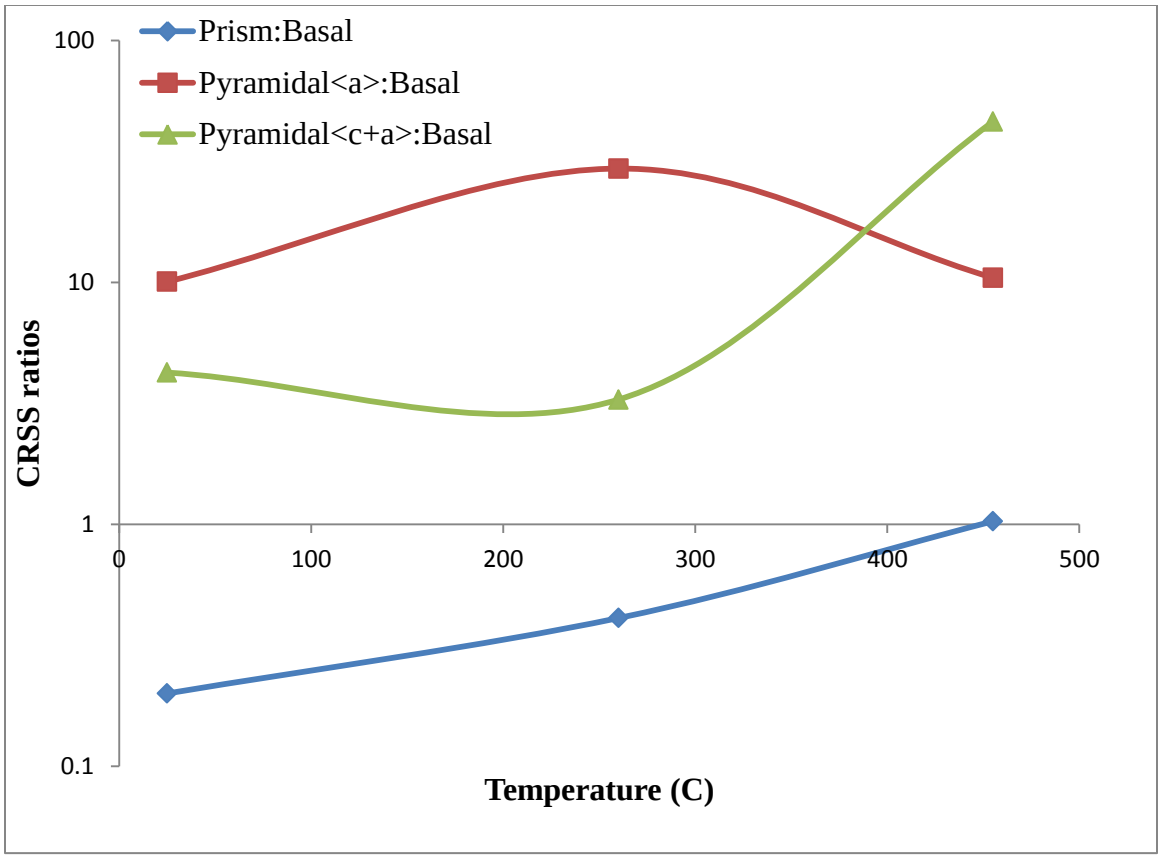

Figure 3.18 Plot of CRSS ratios of prismatic, pyramidal<a>, pyramidal<c+a> to basal slip activities as a function of temperature

For the creep-tests, basal slip activity was dominant under both of the possible testing conditions examined in this work. With increased temperature and decreased stress, the prism: basal CRSS ratio decreased suggesting that prismatic slip becomes more favorable under such conditions. This is to some extent consistent with Li *et al.* [2012] who has also showed that with increased temperature during creep deformation, prismatic slip becomes more dominant.

3.4.3 Comparison of CRSS ratios for Ti-8Al-1Mo-1V with CP Ti and other commercially available Ti alloys

Li [2013] determined the CRSS ratios of the different slip systems for CP Ti, Ti-5Al-2.5Sn, Ti-3Al-2.5V and Ti-6Al-4V at RT and 455^{o}C. Here a comparison of the CRSS ratios of the different slip systems of Ti-8Al-1Mo-1Vis made with those of the above mentioned alloys in Table 3.5.

Table 3.6 Comparison of CRSS ratios of basal, prismatic, pyramidal<a> and pyramidal<c+a> slip activities for Ti-8Al-1Mo-1V with CP Ti and other Ti alloys.

Material	Testing Temp (^{o}C)	Strain (%)	Basal	Prism	Pyramidal<a>	Pyramidal<c+a>
CP Ti	25	4.0	1	0.28	7.1	6.3
CP Ti	455	4.3	1	0.29	5.4	4.7
Ti-5Al-2.5Sn	25	3.5	1	0.81	19.1	35.5
Ti-5Al-2.5Sn	455	4.4	1	1.17	16.7	24.4
Ti-6Al-4V	25	6.3	1	1.2	13.2	38
Ti-6Al-4V	455	3.8	1	1.38	20.2	40.2
Ti-3Al-2.5V	25	10.5	1	0.16	0.81	5.7
Ti-3Al-2.5V	455	16.2	1	0.33	1.1	12.3
Ti-8Al-1Mo-1V	25	3.7	1	0.20	10.07	4.24
Ti-8Al-1Mo-1V	455	9.4	1	1.03	10.46	46.22

The CRSS ratios for prism and basal is 0.2:1 at RT and it changes to 1.03:1 at elevated temperature. So with increased temperature the basal slip activity increased compared to the prismatic slip activity. This is in agreement with the work of Williams *et al.* [2002] who found out that basal slip became more dominant with temperature. Thus it is expected that the CRSS for basal slip decreases more rapidly with increasing temperature compared to prismatic slip. At elevated temperatures, prismatic slip was less favored relative to basal slip, in Ti-8Al-1Mo-1V compared to CP-Ti and Ti-3Al-2.5V. The same is observed when comparing Ti-5Al-2.5Sn and Ti-6Al-4V to CP-Ti and Ti-3Al-2.5V. This is consistent with prior works which suggested that increased Al content increase the *c/a* ratio, which makes the basal plane more close packed and

hence favors basal slip activity [Teer et al. 1977]. Comparison of the prism: basal ratios at different temperatures for all the alloys also suggest that basal slip is more favored with increased temperature.

CHAPTER 4

CONCLUSIONS

1. The material showed a weak texture. The majority of the microstructure contained the α-phase.

2. With increased temperature the CRSS ratio of prism to basal increases from 0.20 to 1.03. At higher temperature the basal activity increased relative to the prismatic slip activity. This work suggested that CRSS for basal slip decreases more rapidly with increased temperature than the CRSS for prismatic slip. Also, during the creep test basal slip was more active than prismatic slip.

3. With increased temperature more grain boundary ledges were observed suggesting an increase in relative amount of GBS. During the creep tests, there was a larger amount of grain boundary ledges suggesting that at lower stresses and elevated temperatures the deformation mechanism changes from dislocation glide to GBS.

4. Cracking occurred during the tensile testing at 455^{o}C and most of the cracks originated at the triple point junctions and grain boundaries. During the elevated-temperature creep testing, cracks nucleated at the triple point junctions or around the grain boundaries. The nature of the cracking was investigated for the 650^{o}C tension test, and suggested to be only localized to the surface of the specimen.

Recommendations for future work

1. In order to better comprehend well the deformation mechanisms in polycrystalline Ti alloys, future work can focus on studying deformation mechanisms in other commercially-available Ti alloys. That will add more data to the literature of the Ti alloys.

2. To have a better understanding of the creep mechanisms, it is necessary to estimate the activation energies of the different mechanisms observed. Future work can focus on performing more creep experiments that will help estimate the activation energies for all the deformation mechanisms observed.

3. To gain a better understanding of the heterogeneous deformation, future *in-situ* tests can be coupled with *in-situ* EBSD mapping. This will help combine grain orientation and surface deformation evolution, which can provide a better understanding of the deformation behavior.

APPENDIX

APPENDIX

The following Matlab code [Li 2013] was used to provide a visual interpretation of the calculated slip traces for all the deformation systems as well as a calculation of the Schmid factors for all the deformation systems for a given orientation. For a particular grain, the input orientation is in the form of three Euler angles ($\phi 1$, Φ, $\phi 2$), given by the EDAX EBSD software. As an example, $\phi 1=47.029$, $\Phi=31.694$, $\phi 2=294.90$. The variable "ssa" contains the 24 common slip systems in Ti, where the slip plane normal directions and slip directions are stored in 24 cells of this variable. In particularly, basal slip systems are stored in cells No.1-3. Prismatic slip systems are stored in cells No.4-6. Pyramidal <a> slip systems are stored in cells No.7-12. Pyramidal <c+a> slip systems are stored in cells No.13-24. In the EBSD coordinate system, since the x-axis is pointing down and y-axis is pointing right, the stress tensor is defined to be [0,0,0;0,1,0;0,0,0]. However, in the lab coordinate system, x-axis is pointing right and y-axis is pointing up, therefore additional 90° degree counterclockwise rotation need to be performed on the calculated slip traces in order to compare the calculated slip traces based on the EBSD coordinate with the SE/BSE images based on the lab coordinate, which is outputted by the Matlab™ code as a figure.

```
% code wrote by Hongmei Li in year 2010 [Li 2013]
clc;
clear;
close
% basal <a>-glide
ssa(:,:,1) = [0 0 0 1; 2 -1 -1 0];
ssa(:,:,2) = [0 0 0 1; -1 2 -1 0];
ssa(:,:,3) = [0 0 0 1; -1 -1 2 0];
% prism <a>-glide
ssa(:,:,4) = [0 1 -1 0; 2 -1 -1 0];
ssa(:,:,5) = [1 0 -1 0; -1 2 -1 0];
ssa(:,:,6) = [-1 1 0 0; -1 -1 2 0];
```

```
% pyramidal <a>-glide
ssa(:,:,7) = [0 1 -1 1; 2 -1 -1 0];
ssa(:,:,8) = [1 0 -1 1; -1 2 -1 0];
ssa(:,:,9) = [-1 1 0 1; -1 -1 2 0];
ssa(:,:,10) = [0 -1 1 1; 2 -1 -1 0];
ssa(:,:,11) = [-1 0 1 1; -1 2 -1 0];
ssa(:,:,12) = [1 -1 0 1; -1 -1 2 0];
% pyramidal <c+a>-glide
ssa(:,:,13) = [1 0 -1 1; 2 -1 -1 -3];
ssa(:,:,14) = [1 0 -1 1; 1 1 -2 -3];
ssa(:,:,15) = [0 1 -1 1; 1 1 -2 -3];
ssa(:,:,16) = [0 1 -1 1; -1 2 -1 -3];
ssa(:,:,17) = [-1 1 0 1; -1 2 -1 -3];
ssa(:,:,18) = [-1 1 0 1; -2 1 1 -3];
ssa(:,:,19) = [-1 0 1 1; -2 1 1 -3];
ssa(:,:,20) = [-1 0 1 1; -1 -1 2 -3];
ssa(:,:,21) = [0 -1 1 1; -1 -1 2 -3];
ssa(:,:,22) = [0 -1 1 1; 1 -2 1 -3];
ssa(:,:,23) = [1 -1 0 1; 1 -2 1 -3];
ssa(:,:,24) = [1 -1 0 1; 2 -1 -1 -3];
euler=[ 47.029 31.694 294.90 ]; % input three Euler angles here
sliptrace=[0,0,0]; % define the calculated sliptrace to be a 1×3 Zero vector
phi1=euler(1,1);
PHI=euler(1,2);
phi2=euler(1,3);
g11=cosd(phi1)*cosd(phi2)-sind(phi1)*sind(phi2)*cosd(PHI);
g12=sind(phi1)*cosd(phi2)+cosd(phi1)*sind(phi2)*cosd(PHI);
g13=sind(phi2)*sind(PHI);
g21=-cosd(phi1)*sind(phi2)-sind(phi1)*cosd(phi2)*cosd(PHI);
g22=-sind(phi1)*sind(phi2)+cosd(phi1)*cosd(phi2)*cosd(PHI);
g23=cosd(phi2)*sind(PHI);
g31=sind(phi1)*sind(PHI);
g32=-cosd(phi1)*sind(PHI);
g33=cosd(PHI);
g=[g11,g12,g13;g21,g22,g23;g31,g32,g33]; %define the rotation matrix
sigma=[0,0,0;0,1,0;0,0,0]; %define the global stress state tensor
c_a=1.59; %define the c/a ratio of Ti

for i=1:1:24 % Change n & m to unit vector
n=[ssa(1,1,i) (ssa(1,2,i)*2+ssa(1,1,i))/3^.5 ssa(1,4,i)/c_a]; % Plane normal of a slip system
m=[ssa(2,1,i)*1.5 3^.5/2*(ssa(2,2,i)*2+ssa(2,1,i)) ssa(2,4,i)*c_a]; % Slip direction of a slip
system
ss(1,:,i) = n/norm(n); % normalization of the slip plane normal direction
ss(2,:,i) = m/norm(m); % normalization of the slip direction
end
```

```
for j=1:1:24 %This loop includes the calculation of plane traces and plotting the plane traces in the coordinate system where x-axis pointing down and y-axis pointing right
plane=ss(1,:,j);
plane=plane';
rot_plane=g'*plane; % rotate slip plane normal direction from the crystal coordinate to lab coordinate
z=[0,0,1];
sliptrace(:,:,j)=cross(rot_plane',z); % perform cross product of the rotated slip plane normal direction and the [001] direction in the lab coordinate
x=sliptrace(1,1,j);
y=sliptrace(1,2,j);
X=[0,x];
Y=[0,y];
axis([-1.2 1.2 -1.2 1.2])
axis square % The figure plotted here need to be counterclockwise rotated by 90 degrees to match the lab coordinate where x-axis is pointing right and y-axis is point up.

if j<4 %This part is to get a prorate number to calculate the space between the slip system labels
k=j;
elseif j<=6
k=j-4;
elseif j<=9;
k=j-5;
elseif j<=12;
k=j-7.5;
elseif j<=15;
k=j-12;
elseif j<=18;
k=j-15;
elseif j<21;
k=j-18;
else
k=j-21;
end

if j>=7 % use black color to plot the calculated plane traces and label the slip system numbers
plot(X,Y,'k'); text(x-0.09*k,y,num2str(j));
else
plot(X,Y,'k'); text(x-0.08*k,y,num2str(j));
end
hold on
end;
for i=1:1:24 % Schmid factor calculation
a=ss(1,:,i);
b=ss(2,:,i);
```

```
schmidfactor(i)=a*sigma*b';
end
rot_c=g'*[0 0 1]'; % This part is to calculate the angle between c-axis of a particular orientation and the tensile direction
angle_C=acosd([0 1 0]*rot_c);
if angle_C>90
angle_C=180-angle_C
else
```

The following MATHEMATICA code [written by Li in 2013] was used to calculate the CRSS ratios for basal :prism:pyramidal<a>:pyramidal<c+a>. The experimental slip data and the raw data from the texture, both as functions of Schmid factor distributions, are given as an input to the code. As an example, in the code below the experimental data and raw texture data for the RT tensile test after a strain of 3.7% are used. The code generates the CRSS ratios of the four different slip systems and the mean and the standard error for each of the three slip systems except the basal slip system, w.r.t the basal slip system.

CRSS Ratio Optimization – Ti811 Alloy - 3.7% strain @ RT

Experimental Data

```
ExperData={{1,2,0,0},{0,1,0,0},{2,0,0,0},{0,0,0,0},{0,0,0,1},{0,1,0,1},{2,3,1,0},{9,3,2,2},{17,13,3,1},{15,19,3,1}}
DiscreteProbData = {};

Do[

 Do[

  Do[

   DiscreteProbData = Append[DiscreteProbData,{i,j}]

   ,{k,1,ExperData[[i,j]]}]


  ,{i,1,10}]
```

```
,{j,1,4}]

(* Generate Histogram of Discrete PDF For Data *)

DataHistGraph = Histogram3D[DiscreteProbData]

(* Generate Discrete PDF for Experimental Data *)

DiscretePDF =EmpiricalDistribution[DiscreteProbData]

DiscretePlot3D[PDF[DiscretePDF,{x,y}],{x,1,10},{y,1,5}, ExtentSize→.8,
ColorFunction→"TemperatureMap", AxesLabel→{"  Schmid Factor  ","","  Probability  "},
Ticks→{{{1,"0.05"},{2,"0.1"},{3,"0.15"},{4,"0.2"},{5,"0.25"},{6,"0.3"},{7,"0.35"},{8,"0.4"},{
9,"0.45"},{10,"0.5"}},{{1,"Basal"},{2,"Prism"},{3,"Pyr <a>"},{4,"Pyr <c+a>"}},{0,.03,.06,
.09,.12,.15}},BaseStyle→{FontWeight→"SemiBold",FontSize→12, FontFamily→"Times New
Roman"} , PlotRange→{0.00001,.16}]
```

Enter and scale texture data for Ti811 Alloy

```
RawSlipSystemData ={{67,46, 106, 212}, {37,54,72,148}, {28,31,56,131}, {23,31,51,111},
{32,31,81, 85},{25,32,70,117},{22, 15,43, 103},{22,17,41,109},{28,18,41,90},{21,25,39,94}};

ListOLD = {};

Do[

  ListNEW = ListOLD;

  ListOLD = Append[ListNEW,RawSlipSystemData[[j]]*((j-1)/9)^3];

  ,{j,1,10}];

ScaledSlipSystemData = ListOLD;

Solution to problem using raw data as a point estimate
CRSSVectorPointEst = {};

Do[

  If[Max[ExperData[[All,j]]]>0,
CRSSVectorPointEst = Append[CRSSVectorPointEst,
N[Sum[ScaledSlipSystemData[[i,j]]^2,{i,1,10}]/Sum[ExperData[[i,j]]*ScaledSlipSystemData[[i,
j]],{i,1,10}]]]; ];
```

```
 ,{j,1,4}];

{CRSSVectorPointEst[[1]]/CRSSVectorPointEst[[1]],CRSSVectorPointEst[[2]]/CRSSVectorPoi
ntEst[[1]], CRSSVectorPointEst[[3]]/CRSSVectorPointEst[[1]],
CRSSVectorPointEst[[4]]/CRSSVectorPointEst[[1]]}
```

Solve minimization problem for Ti811 Alloy at 3.7% strain and RT

```
ResampleNumber = 2000;

ResampleSize = Length[DiscreteProbData];

DivideByZeroCounter = 0;

CRSSList = {};

Do[
 (* Resample Original Data Set *)

 BootstrapData = Table[0,{i,1,10},{j,1,4}];

 Do[

  indexpair = RandomVariate[DiscretePDF];

  BootstrapData =
ReplacePart[BootstrapData,indexpair□BootstrapData[[indexpair[[1]],indexpair[[2]]]]+1];

  ,{j,1,ResampleSize}];


 ExperData = BootstrapData;

 CRSSVector = {};

 (* Compute The Optimal Stress Ratios For Random Sample of Data *)


 Do[

  If[Max[ExperData[[All,j]]]>0,
CRSSVector = Append[CRSSVector,
N[Sum[ScaledSlipSystemData[[i,j]]^2,{i,1,10}]/Sum[ExperData[[i,j]]*ScaledSlipSystemData[[i,
j]],{i,1,10}]]];
```

```
    ,
    DivideByZeroCounter = DivideByZeroCounter+1;
    CRSSVector=Append[CRSSVector, False]];

  ,{j,1,4}];
 CRSSList = Append[CRSSList,CRSSVector];

 ,{i, 1, ResampleNumber}];

Print["Division by 0 was excluded "<>ToString[DivideByZeroCounter]<>" times."];
Generate 3D Histogram of Bootstrapped Dataset
(* Create array "DiscreteData" from Bootstrapped Data set that is \
suitable for the Histogram function in Mathematica *)
DiscreteData = {};
Do[
 Do[
  Do[
    DiscreteData = Append[DiscreteData,{i,j}];
    ,{k,1,BootstrapData[[i,j]]}];

  ,{i,1,10}];
 ,{j,1,4}]

Histogram3D[DiscreteData, ColorFunction→"TemperatureMap", AxesLabel→{"  Schmid
Factor  ","","  Resampled Data\n   (Observations)  "},
Ticks→{{{1,"0.05"},{2,"0.1"},{3,"0.15"},{4,"0.2"},{5,"0.25"},{6,"0.3"},{7,"0.35"},{8,"0.4"},{
9,"0.45"},{10,"0.5"}},{{1,"Basal"},{2,"Prism"},{3,"Pyr <a>"},{4,"Pyr <c+a>"}},{10, 20, 30,
```

```
40}},BaseStyle→{FontWeight→"SemiBold",FontSize→12, FontFamily→"Times New Roman"}]

Histogram3D[DiscreteData, ColorFunction□"TemperatureMap", AxesLabel→{" Schmid Factor "," "," Resampled Data\n (Observations) "},
Ticks→None,BaseStyle→{FontWeight→"SemiBold",FontSize→12, FontFamily□"Times New Roman"}]
```

Generate Resampled Distributions For CRSS ratios

Prism / Basal

Histogram

```
PBCRSSRatioResampledList = {};

UndefinedCounter = 0;

Do[

  If[NumberQ[CRSSList[[i,1]]]&& NumberQ[CRSSList[[i,2]]] ,

    PBCRSSRatioResampledList = Append[PBCRSSRatioResampledList,
CRSSList[[i,2]]/CRSSList[[i,1]]];

    ,

    UndefinedCounter = UndefinedCounter + 1;

    ];

  ,{i,1,ResampleNumber}];

HPDF = HistogramDistribution[PBCRSSRatioResampledList];

PrismBPlot = DiscretePlot[PDF[HPDF,x],{x,Min[PBCRSSRatioResampledList]-
.1*(Max[PBCRSSRatioResampledList]-
Min[PBCRSSRatioResampledList]),Max[PBCRSSRatioResampledList]+.1*(Max[PBCRSSRatioResampledList]-Min[PBCRSSRatioResampledList]),.001},
AxesLabel→{"Prism/Basal","Probability"}, PlotLabel→"Optimal Prism/Basal CRSS - Bootstrapped, N = "<>ToString[ResampleNumber - UndefinedCounter], PlotRange□All,
PlotStyle→Blue, BaseStyle→{FontWeight□"SemiBold",FontSize→26, FontFamily→"Times New Roman"}]
```

```
PrismBPlot = DiscretePlot[PDF[HPDF, x], {x, Min[PBCRSSRatioResampledList] − .1
        ∗ (Max[PBCRSSRatioResampledList]
        − Min[PBCRSSRatioResampledList]), Max[PBCRSSRatioResampledList] + .1
        ∗ (Max[PBCRSSRatioResampledList]
        − Min[PBCRSSRatioResampledList]),.001}, AxesLabel
        → {"Prism/Basal", "Probability"}, PlotRange → All, PlotStyle
        → Blue, BaseStyle → {FontWeight → "SemiBold", FontSize → 34, FontFamily
        → "Times New Roman"}]
```

Resampled Mean & Standard Error

```
PBBootstrapMean = Mean[PBCRSSRatioResampledList]

PBStandardError = Sqrt[Sum[(PBCRSSRatioResampledList[[i]]-
PBBootstrapMean)^2,{i,1,ResampleNumber}]/(ResampleNumber-1)]

Basic Percentage Confidence Interval

Do[

  LeftEndPoint = InverseCDF[HPDF, alpha/2];

  RightEndPoint = InverseCDF[HPDF, 1 - alpha/2];

  PBCIVector = Append[PBCIVector, {LeftEndPoint, RightEndPoint}];

  , {alpha, {.01, .05, .1, .15, .2}}];
```

Basic Bootstrap Interval (per 2010 paper)

```
RatioPointEstimate = CRSSVectorPointEst[[2]]/CRSSVectorPointEst[[1]];

PBBSCIVector = {};

Do[

  LeftEndPoint = 2*RatioPointEstimate-InverseCDF[HPDF,1-(alpha/2)];

  RightEndPoint = 2*RatioPointEstimate-InverseCDF[HPDF,alpha/2];

  PBBSCIVector = Append[PBBSCIVector,{LeftEndPoint, RightEndPoint}];

  ,{alpha,{.01, .05, .1, .15, .2}}];
```

Pyr A / Basal

Histogram

```
PyrABCRSSRatioResampledList = {};

UndefinedCounter = 0;

Do[

  If[NumberQ[CRSSList[[i,1]]]&& NumberQ[CRSSList[[i,3]]] ,

    PyrABCRSSRatioResampledList = Append[PyrABCRSSRatioResampledList,
CRSSList[[i,3]]/CRSSList[[i,1]]];

    ,

    UndefinedCounter = UndefinedCounter + 1;

    ];

  ,{i,1,ResampleNumber}];

HPDF = HistogramDistribution[PyrABCRSSRatioResampledList];

 PyrABPlot
= DiscretePlot[PDF[HPDF, x], {x, Min[PyrABCRSSRatioResampledList] − .1
∗ (Max[PyrABCRSSRatioResampledList]
− Min[PyrABCRSSRatioResampledList]), Max[PyrABCRSSRatioResampledList] + .1
∗ (Max[PyrABCRSSRatioResampledList]
− Min[PyrABCRSSRatioResampledList]),.005}, AxesLabel
→ {"Pyr A/Basal", "Probability"}, PlotLabel
→ "Optimal Pyr A/Basal CRSS − Bootstrapped, N = " <
> ToString[ResampleNumber − UndefinedCounter], PlotRange → All, PlotStyle
→ Red]

(* DiscretePlot[CDF[HPDF,x],{x,0,70,.1}]

DiscretePlot[InverseCDF[HPDF,x],{x,0,1,.01}, PlotRange□All] *)
```

Resampled Mean & Standard Error

```
PyrABBootstrapMean = Mean[PyrABCRSSRatioResampledList]
```

```
PyrABStandardError = Sqrt[Sum[(PyrABCRSSRatioResampledList[[i]]-
PyrABBootstrapMean)^2,{i,1,ResampleNumber-UndefinedCounter}]/(ResampleNumber-
UndefinedCounter-1)]
```

Basic Percentage Confidence Interval

```
PyrABCIVector = {};

Do[

  LeftEndPoint = InverseCDF[HPDF,alpha/2];

  RightEndPoint = InverseCDF[HPDF,1-alpha/2];

  PyrABCIVector = Append[PyrABCIVector,{LeftEndPoint, RightEndPoint}];

  ,{alpha,{.01, .05, .1, .15, .2}}];
```

Basic Bootstrap Interval (per 2010 paper)

```
RatioPointEstimate = CRSSVectorPointEst[[3]]/CRSSVectorPointEst[[1]];

PyrABBSCIVector = {};

Do[

  LeftEndPoint = 2*RatioPointEstimate-InverseCDF[HPDF,1-(alpha/2)];

  RightEndPoint = 2*RatioPointEstimate-InverseCDF[HPDF,alpha/2];

  PyrABBSCIVector = Append[PyrABBSCIVector,{LeftEndPoint, RightEndPoint}];

  ,{alpha,{.01, .05, .1, .15, .2}}];
```

Pyr C+A / Basal

Histogram

```
PyrCABCRSSRatioResampledList = {};

UndefinedCounter = 0;

Do[

  If[NumberQ[CRSSList[[i,1]]]&& NumberQ[CRSSList[[i,4]]] ,
```

```
   PyrCABCRSSRatioResampledList = Append[PyrCABCRSSRatioResampledList,
CRSSList[[i,4]]/CRSSList[[i,1]]];

   ,

   UndefinedCounter = UndefinedCounter + 1;

   ];

 ,{i,1,ResampleNumber}];


HPDF = HistogramDistribution[PyrCABCRSSRatioResampledList];

 PyrCABPlot
 = DiscretePlot[PDF[HPDF, x], {x, Min[PyrCABCRSSRatioResampledList] − .1
 ∗ (Max[PyrCABCRSSRatioResampledList]
 − Min[PyrCABCRSSRatioResampledList]), Max[PyrCABCRSSRatioResampledList]
 + .1 ∗ (Max[PyrCABCRSSRatioResampledList]
 − Min[PyrCABCRSSRatioResampledList]),.005}, AxesLabel
 → {"Pyr C + A/Basal", "Probability"}, PlotLabel
 → "Optimal Pyr C + A/Basal CRSS − Bootstrapped, N = " <
 > ToString[ResampleNumber − UndefinedCounter], PlotRange → All, PlotStyle
 → Blue]

(*
DiscretePlot[CDF[HPDF,x],{x,0,70,.1}]
DiscretePlot[InverseCDF[HPDF, x], {x, 0, 1,.01}, PlotRange → All]*)
```

Resampled Mean & Standard Error

```
PyrCABBootstrapMean = Mean[PyrCABCRSSRatioResampledList]

PyrCABStandardError = Sqrt[Sum[(PyrCABCRSSRatioResampledList[[i]]-
PyrCABBootstrapMean)^2,{i,1,ResampleNumber-UndefinedCounter}]/(ResampleNumber-
UndefinedCounter-1)]
```

Basic Percentage Confidence Interval

```
PyrCABCIVector = {};

Do[

  LeftEndPoint = InverseCDF[HPDF,alpha/2];

  RightEndPoint = InverseCDF[HPDF,1-alpha/2];
```

```
  PyrCABCIVector = Append[PyrCABCIVector,{LeftEndPoint, RightEndPoint}];

  ,{alpha,{.01, .05, .1, .15, .2}}];
```

Basic Bootstrap Interval (per 2010 paper)

```
RatioPointEstimate = CRSSVectorPointEst[[4]]/CRSSVectorPointEst[[1]];

PyrCABBSCIVector = {};

Do[

  LeftEndPoint = 2*RatioPointEstimate-InverseCDF[HPDF,1-(alpha/2)];

  RightEndPoint = 2*RatioPointEstimate-InverseCDF[HPDF,alpha/2];

  PyrCABBSCIVector = Append[PyrCABBSCIVector,{LeftEndPoint, RightEndPoint}];

  ,{alpha,{.01, .05, .1, .15, .2}}];

        PyrCombinedBPlot = Show[PyrABPlot, PyrCABPlot, PlotLabel
                    → "PyrA/Basal (Red) & PyrCA/Basal (Blue)", AxesLabel−
                    > {"CRSS Ratio", "Rel. Prob. "}, BaseStyle → {FontWeight
                    → "SemiBold", FontSize → 20, FontFamily
                    → "Times New Roman"}, PlotRange → {{0,100}, {0,.08}}]
```

BIBLIOGRAPHY

BIBLIOGRAPHY

ASTM, E112-96 standard test methods for determining average grain size, 2004.

Balasubramanian S. and Anand L., Plasticity of initially textured hexagonal polycrystals at high homologous temperatures: application to titanium, Acta Matererilia, Vol. 50, No. 1, pp. 133-148, 2002.

Ball A, Hutchison MM., Superplasticity in the aluminum-zinc eutectoid, Metal Science Journal, Vol. 3, 1969.

Bieler T.R and Semiatin S.L., The origins of heterogeneous deformation during primary hot working of Ti–6Al–4V, International Journal of Plasticity, Vol. 18, No. 9, pp. 1165-1189, 2002.

Boyer R., Welsch G., and Collings E.W., editors. Materials Properties Handbook: Titanium Alloys. Materials Park, OH: ASM International, 1994.

Bridier F., Villechaise P., and Mendez J., Analysis of the different slip systems activated by tension in a α/β titanium alloy in relation with local crystallographic orientation, Acta Materialia, Vol. 53, No. 3, pp. 555-567, 2005.

Burgers W.G., On the process of transition of the cubic-body-centered modification into the hexagonal-close-packed modification of zirconium, Physica, Vol. 1, No. 7-12, pp. 561-586, 1934.

Chan K.S., A micromechanical analysis of the yielding behavior of individual widmanstätten colonies of an α+ β titanium alloy, Metallurgical and Materials Transactions A, Vol. 35, No. 11, pp. 3409-3422, 2004.

Christian J.W. and Mahajan S., Deformation twinning, Progress in Materials Science, Vol. 1995, No.1-2, pp.1-157, 1995.

Clementi E., Raimondi D.L, and Reinhardt W.P., Atomic screening constants from SCF functions, The Journal of Chemical Physics, Vol. 38, No. 11, pp. 2686-2689, 1963.

Dieter G. E. Mechanical Metallurgy, 3rd ed., New York: McGraw-Hill, 1986.

Donachie M.J., Titanium — A Technical Guide (Second Edition) ASM International, OH, USA, 1988.

Dong H. and Li X.Y., Oxygen boost diffusion for the deep case hardening of titanium alloys, Materials Science and Engineering A280, pp 303-310, 2000.

M ES-SOUNI, Creep deformation behavior of three high-temperature near α-Ti alloys: IMI 834, IMI 829, and IMI 685, Metallurgical and Materials Transactions A,Volume 32A, pp. 285-293,2001.
Fisher E.S. and Renken C.J., Single-crystal elastic moduli and the hcp→bcc transformation in Ti, Zr, and Hf, Phys Rev 2A, Vol. 135, No. 2A, pp. 482-494, 1964.

Gollapudi S., Charit I., and Murty K.L., Creep mechanisms in Ti–3Al–2.5 V alloy tubing deformed under closed-end internal gas pressurization, Acta Materialia, Vol. 56, No. 10, pp. 2406-2419, 2008.

Gong J. and Wikinson A.J., Anisotropy in the plastic flow properties of single-crystal α titanium determined from micro-cantilever beams, Acta Materialia, Vol. 57, No. 19, pp. 5693-5705, 2009.

Hayes R.W., Vishwanathan G.B. and Mills M.J., Creep behavior of Ti–6Al–2Sn–4Zr–2Mo: I. The effect of nickel on creep deformation and microstructure, Acta Materialia, Vol. 50, Issue 20, pp. 4953-4963, 2002.

Jenkins W.D. and Williard W.A., Creep rupture properties of Ti-8Al-1Mo-1V alloy, Journal of Research of the National Bureau of Standards-C. Engineering and Instrumentation, Vol. 72C, No. 2, 1968.

Leyens C. and Peters M., Titanium and Titanium Alloys, Fundamentals and Applications, Wiley–VCH GmbH & Co. KGaA , 2003.

Li. H, Analysis of the deformation behavior of the hexagonal close-packed alpha phase in titanium and titanium Alloys, Doctoral Dissertation, 2013.

Li H., Boehlert C.J., Bieler T.R., and Crimp M.A., Analysis of slip activity and heterogeneous deformation in tension and tension-creep of Ti–5Al–2.5Sn (wt%) using in-situ SEM experiments, Philosophical Magazine, Vol. 92, No. 23, pp. 2923-2946, 2012.

Li H., Mason D.E., Bieler T.R., Boehlert C.J., and Crimp M.A., Methodology for estimating the critical resolved shear stress ratios of α-phase Ti using EBSD-based trace analysis, Acta Materialia, Vol. 61, pp 7555-7567, 2013.

Liu Z. and Welsch G., Literature survey on diffusivities of oxygen, aluminum, and vanadium in alpha titanium, beta titanium, and in rutile, Metallurgical Transactions A, Vol. 19A, pp-1121, pp-1121.

Lüthy H., White R.A., and Sherby O.D., Grain boundary sliding and deformation mechanism maps, Materials Science and Engineering, Vol. 39, Issue 2, pp 211-216, August 1979.

Lütjering G. and Williams J.C., Titanium, Springer-Verlag, Berlin, 2003.

Miller W.H., Chen R.T. and Starke E.A., Microstructure, creep and tensile deformation in Ti-6Al-2Nb-1Ta-0.8Mo, Metallurgical Transactions A, Vol. 18, Issue 8, pp 1451-1468, 1987.

Mises R. von, Mechanik der Festen Korper im plastisch deformablen, Math-Phys., Vol. 1, pp. 582-592, 1913.

Okamoto H., Desk Handbook: phase diagram for binary alloys, ASM International, Materials Park Press, 2000.

Paton N.E. and Backofen W.A., Plastic deformation of titanium at elevated temperatures, Metallurgical Transactions A, Vol. 1, Issue 10, pp 2839-2847, 1970.

Salem A.A., Kalidindi S.R., and Semiatin S.L., Strain hardening due to deformation twinning in α-titanium: Constitutive relations and crystal-plasticity modeling, Acta Materialia, Vol. 53, No. 12, pp. 3495-3502, 2005.

Teer D.G. and Salem F.B., The formation of low friction wear-resistant surfaces on titanium by ion plating, Thin Solid Films, Vol. 45, No. 3, pp. 583-589, 1977.

Weiss I., and Semiatin S.L., Thermomechanical processing of alpha titanium alloys-an overview, Materials Science and Engineering A263, pp. 263-256, 1999.

Thiesen KE, Kassner ME, Pollard J, Hiatt DR, Bristow BM, The effect of nickel, chromium, and primary alpha phase on the creep behavior of Ti-6242Si, Metallurgical Transactions A, Vol. 24A, pp. 1819-1826, 1993.

Williams J.C., Baggerly R.G., and Paton N.E., Deformation behavior of HCP Ti-Al alloy single crystals, Metallurgical and Materials Transaction A, Vol. 33, No. 13, pp. 837-850, 2002.

Yoo M.H., Slip, twinning and fracture in hexagonal close-packed metals, Metallurgical Transactions A, Vol. 12, Issue 12, pp 409-418, 1981.

Zaefferer S., A study of active deformation systems in titanium alloys: dependence on alloy composition and correlation with deformation texture, Materials Science and Engineering A, Vol. 344, No. 1-2, pp. 20-30, 2003.

Zeng Z., Zhang Y., and Jonsson S., Microstructure and texture evolution of commercial pure titanium deformed at elevated temperatures, Materials Science and Engineering A, 513-514,pp-83-90, 2009.